2020

NUMERICAL STUDY OF EFFECTS OF WARM OCEAN EDDIES AND OCEANIC BARRIER LAYERS ON TROPICAL CYCLONE INTENSITY IN NORTHWEST PACIFIC

Ilkyeong Ma
University of Rhode Island, ilkyeong_ma@uri.edu

Recommended Citation

Ma, Ilkyeong, "NUMERICAL STUDY OF EFFECTS OF WARM OCEAN EDDIES AND OCEANIC BARRIER LAYERS ON TROPICAL CYCLONE INTENSITY IN NORTHWEST PACIFIC" (2020). *Open Access Master's Theses.* Paper 1914.
https://digitalcommons.uri.edu/theses/1914

NUMERICAL STUDY OF EFFECTS OF WARM OCEAN EDDIES AND OCEANIC BARRIER LAYERS ON TROPICAL CYCLONE INTENSITY IN NORTHWEST PACIFIC

BY

ILKYEONG MA

A THESIS SUBMITTED IN PARTIAL FULFILLMENT OF THE
REQUIREMENTS FOR THE DEGREE OF
MASTER OF SCIENCE
IN
OCEANOGRAPHY

UNIVERSITY OF RHODE ISLAND
2020

MASTER OF SCIENCE THESIS

OF

ILKYEONG MA

APPROVED:

Thesis Committee:

Major Professor Isaac Ginis

Tetsu Hara

Stephen Licht

David C. Smith

DEAN OF THE GRADUATE SCHOOL

UNIVERSITY OF RHODE ISLAND

2020

ABSTRACT

It is well recognized that evaporation from the sea surface, primarily within a tropical cyclone (TC) core, provides heat energy required to maintain and intensify the storm. The sea surface temperature (SST) typically decreases within the storm core due to the mixing and upwelling processes in the upper ocean thereby limiting the storm intensity. This negative feedback to the TC intensity depends on the oceanic thermal conditions and salinity stratification ahead of the storm. Upper oceanic heat content (OHC) has become widely accepted as a measure of the ocean energy available to the TCs. Observational and modeling studies note that some TCs rapidly intensify while passing over warm core eddies (WCEs) because of their high OHC. TC intensification is also significantly affected by salinity-induced barrier layers (BLs) formed when a low-salinity is situated near the surface in the upper tropical oceans. When storms pass over the regions with BL, the increased stratification and stability within the layer reduce storm-induced vertical mixing and SST cooling. This causes an increase in enthalpy flux from the ocean to the atmosphere and, consequently, leads to TC intensification. In this study, we applied the Hurricane Weather Research and Forecast (HWRF) v.4.0 system coupled to the Message Passing Interface Princeton Ocean Model (MPIPOM). We conducted the idealized experiments in which the WCE is embedded into the U.S. Navy's Generalized Digital Environmental Model (GDEM) climatology with a specified size using a feature-based initialization procedure. Idealized vertical ocean profiles from Hlywiak and Nolan (2019) are selected to conduct the sensitivity of TC intensity to BL thickness. The goal of this study is to quantify the impact of WCEs

and BLs in the upper ocean on TC's self-induced cooling and subsequent feedback on TC intensity in three TCs in 2018, Jebi, Trami, and Kong-Rey

ACKNOWLEDGMENTS

First, I would like to thank my major advisor, Dr. Isaac Ginis, for the guidance and support to finish this degree at the Graduate School of Oceanography. I also thank my thesis committee members, Dr. Tetsu Hara and Dr. Stephen Licht for their help on this latest step in my academic journey. I am very grateful to my lab mates, Mansur Ail Jisan, Xiaohui Zhou, and Xuanyu Chen for helping me through graduate school and providing helpful advice. To David Smith, Meredith Clack, and Jane Eaton, thank you for your support in navigating a coherent path to graduation. I also thank the National Center for Atmospheric Research (NCAR) for the use of their computing resources. Lastly, to my funding sources, Korea Institute of Ocean Science and Technology (KIOST), thank you for providing the opportunity to attend GSO and complete my research.

TABLE OF CONTENTS

LIST OF TABLES

LIST OF FIGURES

Chapter 1

Introduction

Tropical cyclones (TCs), known as hurricanes or typhoons, form over warm water in tropical oceans, especially in late summer, and cause devastating disasters such as heavy rains, floods, and storm surges resulting in immense damages in social and economic aspects. It has been well known that heat energy from the upper ocean is a source to generate and intensify the TCs (Emanuel et al., 1986; Cione and Uhlhorn, 2003). In the development of TC, the surface wind stress leads to an increase of evaporation from the sea surface, and it provides the latent heat energy to develop the TC. The surface water is, however, cooled by the imposed surface wind stress as the storm continues to intensify, which results in a decrease in the heat energy from the ocean surface and weakens the storm's intensity (Shay et al., 2000; Bender and Ginis, 2000). Sea surface cooling is generated during the evaporation, but the main cooling processes are caused by the wind stress via shear-induced turbulent mixing of the upper ocean, upwelling and entrainment from the deep ocean into the oceanic mixed layer (Price 1981; Shen and Ginis, 2003; D'Asaro et al., 2007). It is evident that the magnitude of the sea surface cooling near the storm core contributes to the TC intensity. However, negative feedback from sea surface cooling to TC intensity is not merely exerted by storm forcing, but the combination with ocean thermal conditions (Price 1981; Schade and Emanuel, 1999; Bender and Ginis, 2000; Chan et al., 2001; Lin et al., 2005; Jaimes et al., 2015; Wang et al., 2018). Generally, the sea surface cooling is inhibited by a thicker subsurface warm water layer during the passage of the storm as the cold water from deep cannot be entrained into the surface layer. This results in a less sea surface temperature (SST) cooling that can potentially strengthen the storm intensity if all else being equal. Thus, understanding the upper ocean thermal structure plays a crucial role in examining storm intensification because TCs interact not only with the surface waters but with the entire upper ocean water column.

Warm core eddies (WCEs), which have a characteristic of higher temperatures than the surrounding waters with downwelling motion in the eddy regime, are the common mesoscale features in the ocean. WCE has been regarded as an insulator between TCs and the deep ocean water in that the thicker mixed layer in the WCE can limit the wind-induced mixing of the upper ocean from below (Lin et al., 2005). WCE can reduce the negative feedback and help to transport sufficient heat energy into the storm to intensify. Thus, understanding the interaction of TCs with WCE is critical for improving the understanding and prediction of the TC intensity change. Recent studies have identified that TC intensifications occur when passing over the WCEs (Hong et al., 2000; Shay et al., 2000; Emanuel et al., 2004; Lin et al., 2005; Wu et al., 2007; McTaggart-Cowan et al., 2007; Vianna et al., 2010; Yablonsky and Ginis, 2013; Jaimes et al., 2016). Lin et al. (2005) discussed the importance of WCE in Typhoon Maemi, which rapidly intensified from category 3 to category 5. Maemi intensified while passing over two WCEs in the northwest Pacific and became one of the most powerful Typhoons to strike South Korea since record keeping began in the country in 1904.

Northwest Pacific is well known as one of the most active TC basins in the world (Emanuel., 2005; Peduzzi et al., 2012; Lin et al., 2013) and the region where eminent WCEs exist, particularly in the eddy-rich zones (Qiu 1999; Roemmich and Gilson, 2001; Hwang et al., 2004; Lin et al., 2005). In this study, we focus on the interaction between WCEs and TCs in the southern eddy zone (18°–25°N, 122°–160°E) where Maemi intensified over WCEs (Fig. 1.1). Previous studies conducted analyses of the WCEs in this region (Liu et al., 2012; Yang et al., 2013; Ma et al., 2017). According to Liu et al. (2012), the average size (radius) of anticyclonic eddies is 120–140 km at the latitude of 20°N in the southern eddy zone (Fig. 1.2).

There have been many studies investigating the impact of WCE on the TC, however, most of the previous modeling studies are based on a single storm case (Hong et al., 2000; Shay et al., 2000; Lin et al., 2005; Wu et al., 2007; Jaimes and Shay, 2015; Wang et al., 2018) or using simple one-dimensional ocean models (Chan et al., 2001; Lin et al., 2005; Wu et al., 2007). For the TC prediction model to capture the effect of wind-induced sea surface cooling, it must be fully coupled to a three-dimensional ocean model to create an accurate SST field (Yablonsky and Ginis, 2009). In recent years, numerical atmosphere-ocean coupled models have been used to explore the impact of WCE on TC intensity. Yablonsky and Ginis (2013) suggested that the circulation of WCE can affect the TC intensity, and the WCE located to the right of the storm could even cause a less favorable condition for TC intensification due to the advection of cold water into the TC inner core. Ma et al. (2017) suggested that the effect of ocean eddies is related to the strength of eddy and TC intensity, and the effect is less pronounced when the eddy is located at one side of storm tracks than at the TC center. Anandh et al. (2020) showed that eddies play an important role in the intensification and dissipation of TCs in the Bay of Bengal using an atmosphere-ocean coupled numerical model, consisting of the Weather Research and Forecast (WRF) and Regional Ocean Modeling Systems (ROMS). Sun et al. (2020) investigated the response of TC intensity change to the spatial distribution of WCE using WRF and the three-dimensional Price-Weller-Pinkel (3DPWP) ocean circulation model. The results revealed that TC is strongly intensified (weakened) with a WCE located in the inner (outer) TC eyewall area. All of these modeling studies have been conducted for idealized TCs and simplified ocean conditions. The impact of WCEs on storm-induced ocean response and TC intensity in a realistic environmental setting remains unexplored by numerical models.

Negative feedback from the ocean, which reduces TC intensification depends on the ocean thermal parameters as well as the upper ocean stratification. There are regions where a low-salinity water is located near the surface, and these low-salinity layers can induce barrier layers (BLs) when the isothermal layer is deeper than the mixed layer (Lukas and Lindstrom, 1991; Sprintall and Tomczak, 1992). BL can increase stratification in the upper ocean, and thereby reduce the surface cooling negative feedback on TC intensity. When a TC passes over a region with the BL, the increased stability within the upper ocean layer can reduce TC-induced vertical mixing. This causes a decrease in SST cooling and an increase in enthalpy flux from the ocean to the atmosphere and consequently leads to TC intensification. Previous studies have examined how the SST response to the TC-induced wind is affected by the BL (Wang et al., 2011; Balaguru et al., 2012; Vissa et al., 2013; Reul et al., 2014; Hernandez et al., 2016; Yan et al., 2017; Rudzin et al., 2018; Hlywiak and Nolan, 2019). Balaguru et al. (2012) discussed the impact of BL on the reduction of SST cooling and TC intensification on a global scale. One of the well-known regions where the BLs form is the Amazon-Orinoco river plume region. Previous studies found that the TC-induced vertical mixing and SST cooling significantly are inhibited over the plume area due to the presence of strong vertical stratification (Grodsky et al., 2012; Reul et al., 2014). However, the recent studies of Newinger and Toumi (2015) and Hernandez et al. (2016) found that there was little difference in TC-induced cooling between the plume and open ocean experiments using a regional ocean model. Yan et al. (2017) showed that the BL can weaken the storm intensity when the surface wind stress is too weak to break through the mixed layer. Hlywiak and Nolan (2019) conducted idealized simulations using an atmosphere-ocean coupled model. Their results revealed that for TCs of greater than Category 1 intensity, thick (24–30 m) BLs favor TC intensification by 6–15%, and conversely, weaker storms are hindered by thick barrier layers.

Previous studies explored relationships between upper ocean salinity stratification in the form of oceanic BLs and TCs based on observations, which can be sparse or incomplete or idealized numerical models. Here, we provide an approach to the problem by directly exploring the intensification of TCs over BL regions using a fully atmosphere-ocean coupled model in real TCs. This study is part of the Ocean-Typhoon Interaction at Korea Institute of Ocean Science & Technology (KIOST) (Fig. 1.3). The purpose of project is to investigate TC's rapid intensification processes through observations and numerical models of air-sea interaction.

The goal of this study is to quantify the impact of WCEs and BLs in the upper ocean on TC's self-induced cooling and subsequent feedback on TC intensity in three TCs in the northwest Pacific in 2018, Jebi, Trami, and Kong-Rey. Chapter 2 gives the model description and properties of the three TCs. The impact of WCEs on TC intensity is examined in Chapter 3. The impact of the BL on TC intensity is discussed in Chapter 4.

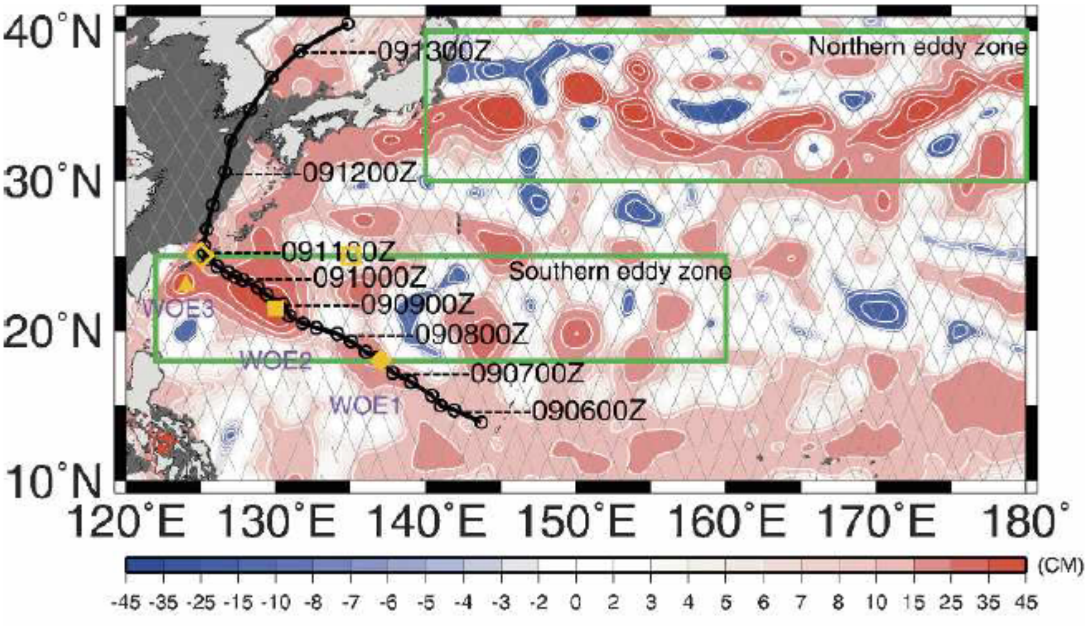

Figure 1.1. Composite of NASA's TOPEX/Poseidon and Jason-1 altimetry measure ments between 27 August and 5 September 2003 showing the pre-Maemi SSHA. Maemi's track and locations of the two eddy-rich zones (northern eddy zone and southern eddy zone) are overlaid (Lin et al., 2005).

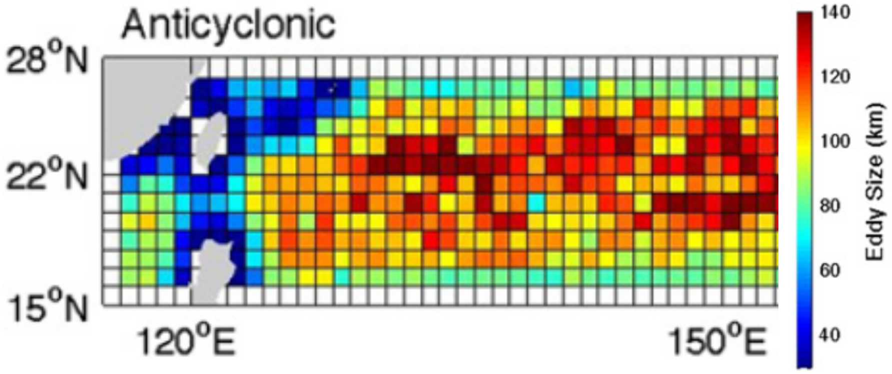

Figure 1.2. Spatial distribution of averaged anticyclonic eddy (WCE) size (km) over 1° x 1° bins from 1993 to 2010 (Liu et al., 2012).

KIOST
KOREA INSTITUTE OF
OCEAN SCIENCE & TECHNOLOGY

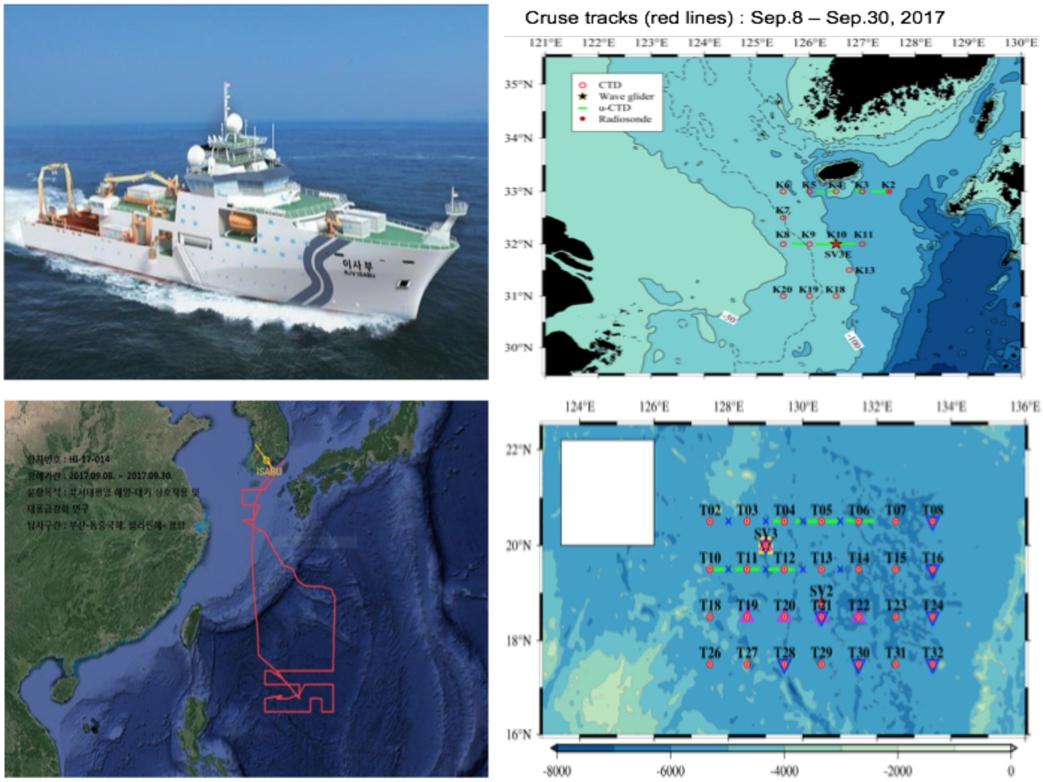

Figure 1.3. (Left) Korea Institute of Ocean Science & Technology (KIOST) research vessel, its path for over 2 weeks on September 2017 in the northwest Pacific and (right) CTD deployment locations.

Chapter 2

Methodology

2.1 Model Description

2.1.1 HWRF Model

Numerical experiments are performed using the Hurricane Weather Research and Forecast (HWRF) – NOAA's operational hurricane prediction model. HWRF is an atmosphere-ocean coupled model, employing a suite of advanced physical parameterizations for tropical cyclones applications. HWRF became operational in 2007, working in collaboration with the Geophysical Fluid Dynamics Laboratory (GFDL) of National Oceanic and Atmospheric Administration (NOAA) and the University of Rhode Island (URI) (Tallapragada et al., 2014). The HWRF system is implemented at the National Centers for Environmental Prediction (NCEP) of the National Weather Service (NWS) to provide numerical guidance to the National Hurricane Center (NHC) for 126 h forecasts of TCs' track, intensity, and structure. The version of HWRF used in this study is the 2018 operational HWRF, version 4.0a, which has three nested atmospheric domains, one fixed parent domain and two inner movable domains, with horizontal grid spacings of 13.5, 4.5, and 1.5 km (Fig. 2.1). The location of the parent domain is determined based on the initial position of the storm and the NHC and Joint Typhoon Warning Center (JTWC) forecasts of the 72h position, if available (Biswas et al., 2017).

2.1.2 Ocean Model

The atmospheric component of the HWRF is coupled to a three-dimensional version of the Princeton Ocean Model (POM; Mellor 2004), called POM for Tropical Cyclones (POM-TC; Yablonsky et al., 2015b). To increase the resolution of POM-TC and provide the framework for flexible ocean initialization options, POM-TC has been replaced in HWRF with a new, Message Passing Interface (MPI) version of POM-TC, called MPIPOM-TC (Yablonsky et al., 2015b). Calculations are performed on a staggered Arakawa C-grid with curvilinear orthogonal coordinates. The horizontal domain spans from 10° to 47.5° North meridionally and from 98.5° to 15.3° East zonally, with roughly 1/12 resolution. The vertical coordinate is the terrain-following sigma coordinate system (Mellor 2004). In this study, 40 half-sigma vertical levels of the original MPIPOM are increased to 74 levels to allow for a finer vertical resolution in the upper ocean (Fig. 2.2). There are 74 half-sigma vertical levels, where the level placement is scaled based on the bathymetry of the ocean at a given location. The greatest vertical spacing occurs where the ocean depth is 5500 m. The 74 full-sigma vertical levels are located at 0, 2, 4, 6, 8, 10, 12, 14, 16, 18, 20, 22, 24, 26, 28, 30, 32, 34, 36, 38, 40, 42, 44, 46, 48, 50, 52, 54, 56, 59, 61, 63, 66, 68, 71, 74, 77, 81, 85, 89, 94, 100, 107, 115, 125, 136, 149, 164, 183, 204, 230, 260, 296, 337, 387, 444, 511, 590, 682, 788, 912, 1055, 1220, 1411, 1630, 1882, 2171, 2501, 2878, 3308, 3797, 4352, 4981, and 5500 m depths. The Mellor–Yamada turbulence closure scheme (Mellor and Yamada, 1982) is embedded in the model to provide vertical mixing coefficients.

2.2 Running HWRF

2.2.1 Ocean Model Initialization

Prior to the coupled model integration of the HWRF system, MPIPOM-TC is initialized with a realistic, three-dimensional temperature and salinity field from the Generalized Digital Environmental Model (GDEM) monthly climatology (GDEMv3; Carnes 2009), which has a 0.5° horizontal grid spacing and 78 vertical z levels and subsequently integrated to generate realistic ocean currents (Teague et al., 1990). The GDEM climatology is modified by interpolating it in time to the MPIPOM-TC initialization date (using 2 months of GDEM) and onto the MPIPOM-TC grid, assimilating a land/sea mask and bathymetry data (Falkovich et al., 2005; Yablonsky and Ginis, 2008). The ocean temperature field is generated after assimilating with the real-time daily SST data (with 1° grid spacing) that is used in the operational NCEP Global Forecast System (GFS) global analysis (Reynolds and Smith, 1994; Yablonsky and Ginis, (2008, section 2)). Three-dimensional ocean initial temperature and salinity fields are then interpolated from GDEMv3 levels onto MPIPOM-TC vertical sigma levels. During the ocean spin up of 48 h in phase 1, the SST is held constant, and adjusted currents are generated. During phase 2, a cold wake at the sea surface is produced prior to the start of the coupled model forecast. Phase 2 is skipped in this study and the output after spin-up is used for the initial ocean component of the HWRF model.

2.2.2 Atmospheric Model Initialization

The location of the HWRF atmospheric component parent and inner domains is based on the observed TC's current and center position based on the NHC storm message. Once the environment fields in the parent domain are derived from interpolating the GFS analysis fields, the vortex replacement cycle and HWRF Data Assimilation System (HDAS) are used to create the initial nest fields (Domain size for parent nest is 77°x77°, inner nest 1 is 20°x20°, and 11°x11° for inner nest 2). The vortex-scale fields are generated by inserting a vortex corrected using TC vitals data (Trahan and Sparling, 2012). The analyses are interpolated onto the HWRF outer domain and two inner domains to initialize the forecast. (Tallapragada et al., 2014).

2.2.3. Coupled Model Run

After the ocean and atmosphere initializations are completed, the coupled HWRF is launched. During the atmosphere-ocean coupling, the momentum fluxes and total heat at the air-sea interface are passed from the atmosphere to the ocean, and the SST is passed from the ocean to the atmosphere as an independent interface between the HWRF ocean and atmospheric component (Fig 2.3). It highlights that the primary purpose of coupling a three-dimensional ocean model to HWRF is to create an accurate SST field for input into the atmospheric model. The total simulation time is 126 h and the output is provided every 6 hours.

2.3 Simulated Tropical Cyclones in the Northwest Pacific

Numerical simulations of three TCs, Jebi, Trami, and Kong-Rey, all occurred in 2018 in the northwest Pacific are conducted. TC Jebi formed near the Marshall Islands in Western Pacific on 26 August and quickly strengthened as it headed west and rapidly underwent rapid intensification and became a super typhoon. Jebi is reported as the most intense TC to make landfall on Japan since TC Yancy in 1993, causing significant damage. Jebi reached its peak intensity as a Category 5, with 10-minute sustained winds of 195 km/h and a minimum pressure of 915 hPa. TC Trami developed in a low-pressure area southeast of Guam on 20 September and intensified into a TC on 22 September. Trami steadily strengthened and subsequently became a Category 5 TC on 24 September. After that, Trami considerably slowed down and drifted northward and during this time, it began to weaken due to upwelling. TC Kong-rey originated from a tropical disturbance in the open Pacific and became TC on 30 September. Kong-rey continued to strengthen into a powerful Category 5 super typhoon early on 2 October. Later, affected by vertical wind shear, low ocean heat content, and decreasing sea surface temperatures, the storm gradually weakened to a Category 3 typhoon on 3 October and made landfall in South Korea.

Four sequential experiments are conducted for each TC at 6-hour intervals: from 0600 UTC 30 August to 0000 UTC 31 August for Jebi, from 1200 UTC 23 September to 0600 UTC 24 September for Trami, and from 1800 UTC 30 September to 1200 UTC 1 October for Kong-rey. The initial times for the experiments are selected in such a way that the simulated HWRF TC tracks and intensities (i.e., Maximum 10 m wind speed and minimum central pressure) are most consistent with the observational data (BEST) (https://www.emc.ncep.noaa.gov/gc_wmb/vxt/HWRF/). The BEST tracks are data files that contain a complete history of the storm’s center locations, intensity, and other parameters using information found in the TCvitals that the U.S. Navy's Joint Typhoon Warning Center (JTWC) provides to the U.S. National Oceanagraphic and Atmospheric Administration's National Center for Environmental Prediction (NOAA/NCEP) for the purpose of initializing the model (http://hurricanes.ral.ucar.edu/realtime/index.php#

about_bdecks). Figure 2.4 shows the BEST tracks of three storm and the time series of translation speed (m/s) is shown in Fig. 2.5. Translation speed is determined every 6 h from the initial time until landfall for each storm using centered difference calculations of storm center positions. The simulated tracks and intensities will be presented in Chapters 3 and 4.

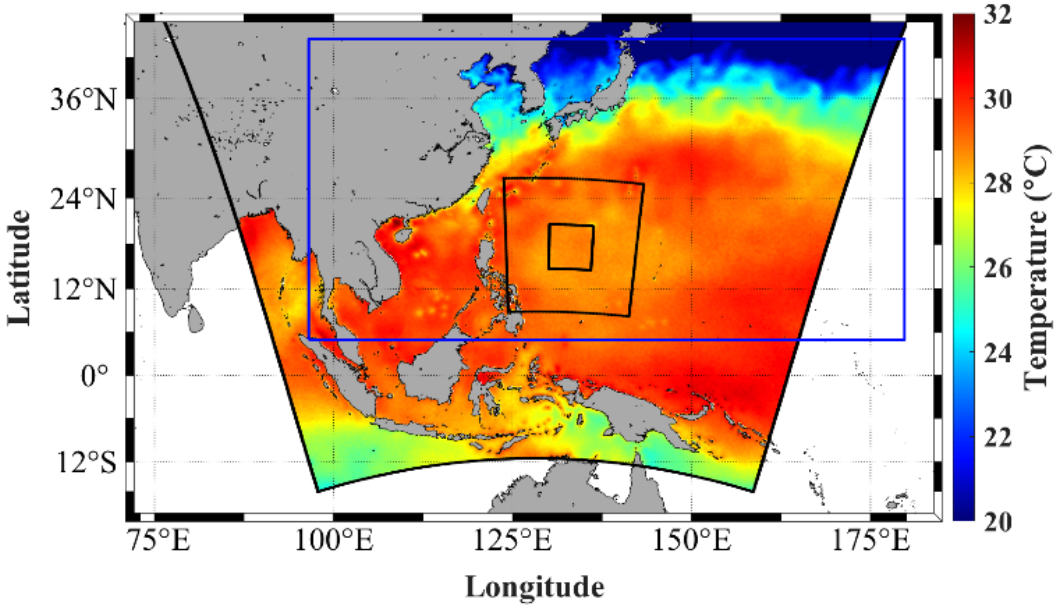

Figure 2.1. HWRF model forecast domains. The region with SST is the outer 13.5 km domain. The black solid boxes inside show the sizes of the vortex-following 4.5 and 1.5 km domains, respectively. The blue box is the Western Pacific MPIPOM-TC domain.

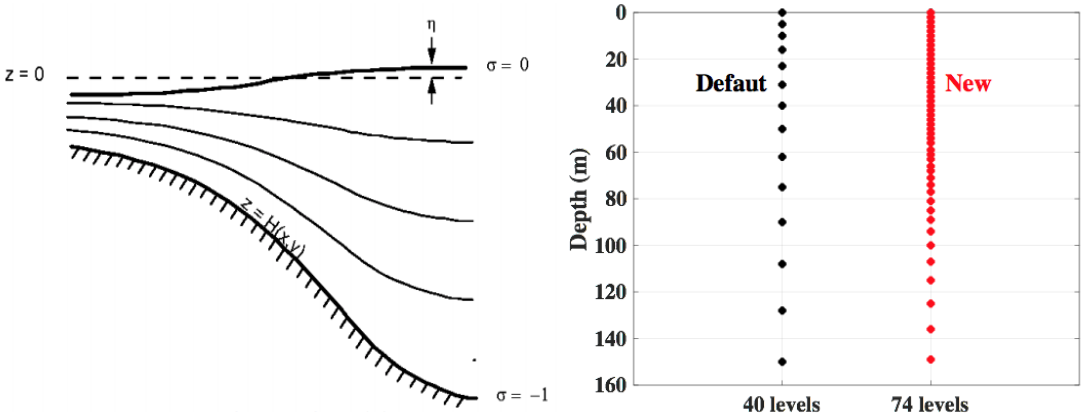

Figure 2.2. Diagram of the vertical sigma coordinate (left). A comparison of sigma level distribution in MPIPOM (right) in the upper 160 m in the 40 level (black dots) and 74 level (red dots) regimes. Location of sigma levels is at 5500 m.

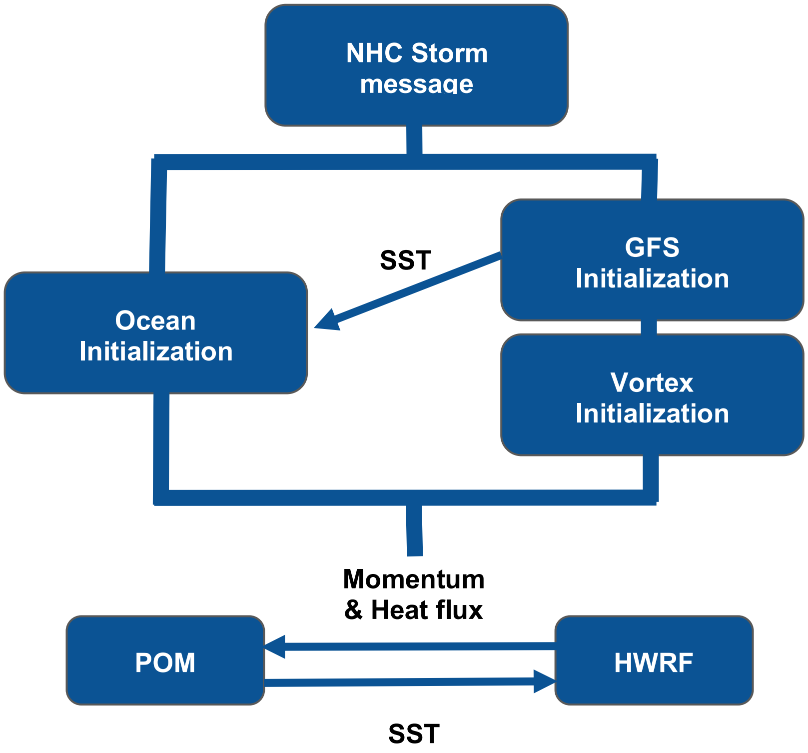

Figure 2.3. Simplified overview of the HWRF system.

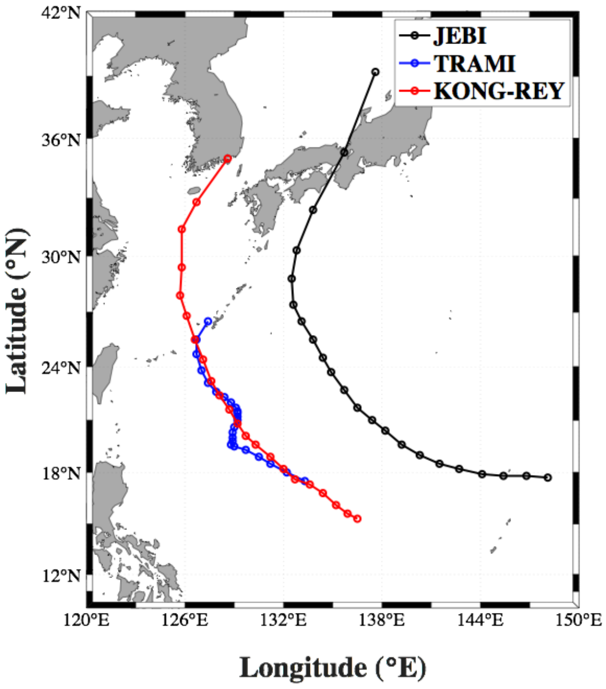

Figure 2.4. BEST tracks of TC Jebi (black), Trami (blue), and Kong-rey (red). Circles indicate the storm center every 6 hours.

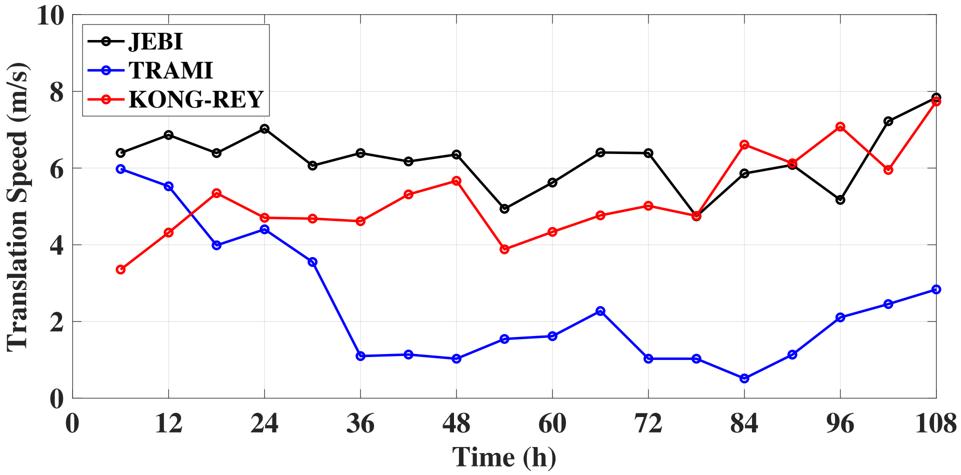

Figure 2.5. Translation speed of TC Jebi (black), Trami (blue), and Kong-rey (red) every 6 hours as a function of time.

Chapter 3

Impact of Warm Core Eddies on TC Intensity

3.1 Initialization and Experiment Design

In the control experiment (CTRL), the ocean is initialized with the GDEM climatology and the real-time daily GFS SST. To compare the impact of the WCE with the same Coriolis effects on the TCs, which have different characteristics, WCE is implemented at the same latitude for all storm cases positioning at the center of each storm track. Under each of three TCs, simulations are run with: No WCE (temperature and salinity climatology), with WCE (salinity climatology). Idealized WCEs are embedded into the three-dimensional GDEM temperature climatology. WCEs are created using the specified temperature profile depicted in Lin et al. (2005) and sea surface height anomalies (SSHA) using the feature-based methodology described in Yablonsky and Ginis (2008) (Fig. 3.1). The SSHA data is provided by the Archiving Validation and Interpretation of Satellite Data in Oceanography (AVISO), which merges the altimeter missions of the Ocean Topography Experiment (TOPEX) /Poseidon, Jason-3, Sentinel-3A, HY-2A, Saral/AltiKa, Cryosat-2, Jason-2, Jason-1, ENVISAT, GFO, ERS1/2 with a spatial resolution of 1/4° x 1/4°. Specifically, AVISO SSHA data on 21 September 2017 is used to determine the spatial structure and magnitude of WCE (Fig. 3.1a).

The upper ocean temperature profiles at the center of WCE and the background are shown in Fig. 3.1b. The temperature profile of the WCE center is from the most prominent WCE that super typhoon Maemi passed over and intensified (Lin et al., 2005). The background profile is from GDEM climatology at the location where the

WCE is implemented. The WCE center profile in Lin et al. (2005) was provided by the U.S. Naval Research Laboratory's NPACNFS nowcast model, which is the ocean model with near real-time operational assimilation of satellite observations. The WCE is initialized by assigning a series of specified temperatures from the background temperature profile to the WCE center (Yablonsky and Ginis, 2008; Yablonsky and Ginis, 2013). The horizontal temperature field in WCE at 75 m depth and the zonal vertical cross section after the initialization are shown in Fig. 3.2. The radius of the idealized WCE is set to be about 200 km based on the observed SSHA shown in Fig. 3.1a. In this study, the size of eddy is defined to be the radius of the circle that has the same area as the region within the eddy edge, and the outmost closed SSHA contours are used to define the eddy edge. After the WCE is created, a temperature anomaly field is obtained by subtracting the background temperature. The anomaly field is horizontally interpolated onto the POM grid and added to the GDEM climatology in such a way that the simulated storm track crosses the center of WCE. Figure 3.3 illustrates the WCE embedding procedure for TC Kong-rey. Additional experiments with different sizes of WCE are performed to quantify the impact of WCE sizes on storm intensity. In these experiments, WCE are initialized with a radius of 140 km, a typical size in the southern eddy zone in northwest Pacific, and a radius of 300 km, similar to the size of the most intense WCE described in Lin et al. (2005). Fig. 3.4 shows the WCEs of the 140 and 300 km radii embedded in the same location as in Fig. 3.3.

3.2 Control Experiments

Before comparing the results between CTRL and WCE experiments, it is important to first investigate the results of each CTRL experiment to examine the different characteristics of each storm, interacting with the different ocean conditions. Here we compare the control experiments initialized at 0600 UTC 30 August for Jebi, 1200 UTC 23 September for Trami, and 1800 UTC 30 September for Kong-rey. In Kong-rey CTRL experiment, the storm rapidly intensified during the first 12 hours as seen in the increased maximum wind speed and decreased central pressure (Fig. 3.5). Figure 3.6a shows the spatial distribution of pre-storm SST with the storm track. Kong-rey passes the warmer ocean surface in the first 24 hours. However, relatively uniform SST distribution along the track does not explain the initial rapid intensification, and thereby upper the ocean thermal structure and the upper ocean heat content need to be explored. Upper ocean heat content (OHC, also known as tropical cyclone heat potential) is the integrated heat content, excess relative to the 26°C, from the depth of 26°C isotherm to the surface and, can be calculated as follow:

$$OHC = \int_0^{d26} \rho c_p [T(^\circ\mathrm{C}) - 26] dz \qquad (1)$$

where $d26$ is the depth of the 26°C isotherm, ρ is the seawater density, c_p is a specific heat at constant pressure, T is the ocean temperature, and dz is the change in depth (Leipper and Volgenau, 1972). We assume a constant density of 1025 $\mathrm{kg/m^3}$ for our calculations. Considerably high OHC of around 100 $\mathrm{kJ/cm^2}$ at the beginning of Kong-rey track indicates more heat energy available for the storm and explains the initial rapid intensification (Fig. 3.6b). This is consistent with previous studies proposed that SST in advance of the TC does not account for the storm-induced SST cooling, and OHC ahead of the storm is a better measure of the available ocean energy for TC intensification (Shay et al., 2000; Mainelli et al., 2008).

In the Jebi CTRL experiment, the pre-storm SST field is around 30°C along the track which is higher than that in Kong-rey (Fig. 3.8a). As for Kong-rey, the evolution of Jebi intensity (Fig. 3.7) can be interpreted by the distribution of the OHC field rather than SST. The gradual intensity increase at the early stage occurs as the storm passes over the high OHC region during the first two days (Fig. 3.8b). The maximum wind speed decreases from 1800 UTC 2 September until landfall at 1200 UTC 4 September due to the lower OHC along the track. In the Trami CTRL experiment, there is a significant intensity decrease in the middle of the simulation (Fig. 3.9). This is because the Trami propagated with a very slow translation speed during that time period. Figure 3.10 compares the distribution of SST and a zonal vertical cross section along 20.4°N at 1800 UTC 23 September and 1200 UTC 26 September. The slow TC propagation speed generates strong vertical mixing as well as upwelling. Vertical mixing occurs due to wind stress driven ocean currents and the resulting vertical current shear leading to entrainment of the colder water from thermocline into the ocean surface layer (Price 1981; Ginis 2002). Ocean surface currents are also diverged by the TC cyclonic wind stress above causing the upwelling of the colder water toward the surface and making thermocline to lift (Fig 3.10d). The TC induced upwelling increases the efficiency of the vertical mixing and cooling of the SST. This explains why TC Trami rapidly weakened.

3.3 Uncoupled Experiments

In addition to the atmosphere-ocean coupled simulations, uncoupled TC model experiments are performed with a static (fixed in time) SST field to compare the results with the CTRL and WCE experiments. Four experiments are conducted in each TC case at 6-hour intervals, from 0600 UTC 30 August to 0000 UTC 31 August for Jebi, from 1200 UTC 23 September to 0600 UTC 24 September for Trami, and from 1800 UTC 30 September to 1200 UTC 1 October for Kong-rey. The storm tracks in the uncoupled and CTRL simulations are compared in Fig 3.11, and the intensity evolutions in each storm case measured by TC minimal central pressure are compared in Figs. 3.12 (Jebi), Fig. 3.13 (Trami), and Fig. 3.14 (Kong-rey). Despite similar tracks between the coupled and uncoupled simulations, the evolutions of TC intensity are remarkably different in all three TCs. This is because the fixed SST does not account for TC-induced SST cooling and thus provides unlimited heat energy for TC intensification. Therefore, we will use the uncoupled simulations as a reference for the maximum potential intensity that can be attained by each storm. The maximum differences between area-averaged values of the sea surface temperature (SST), heat flux (HT), minimum pressure (Pmin), and maximum wind (Vmax) within 100 km of the storm center (the storm core region) in the uncoupled and CTRL experiments are summarized in Table 1. As expected, the largest differences are found in TC Trami, which is the slowest-moving storm among the three simulated TCs (Fig. 2.5). The slow translation speed in Trami allows sufficient time to mix and cool the upper ocean beneath the storm, which is the largest within the storm core. This leads to the largest differences in maximum SST, heat flux, and intensity compared to the uncoupled, fixed SST, experiments.

3.4 Impact of Warm Core Eddy on TC intensity

Here we discuss the TC simulations in which the ocean model is initialized with an embedded WCE. As in the CTRL and uncoupled simulations, four experiments are conducted in each storm case at 6-hour intervals, from 0600 UTC 30 August to 0000

UTC 31 August for Jebi, from 1200 UTC 23 September to 0600 UTC 24 September for Trami, and from 1800 UTC 30 September to 1200 UTC 1 October for Kong-rey. In each experiment, WCE is placed at the same latitude (20.4°N) and in such a way that its center is positioned on the TC track to examine the maximum impact on storm intensity. We first discuss the results of TC Jebi initialized on 0600 UTC 30 August, TC Trami initialized on 1200 UTC 23 September, and TC Kong-rey initialized on 1800 UTC 30 September. To quantify the impact of WCE on the TCs, the area-averaged values are calculated within a 100 km radius at the storm center for each storm simulation (Figs 3.15, 3.16, and 3.17). The vertical red dashed lines indicate the time during the storm is passing over the WCE. This period is determined by the time from when the storm's radius of maximum wind (RMW) enters and exits the WCE area. As the storm passes over the WCE ocean surface cooling is decreased by the WCE, and hence more heat energy can be provided from the ocean to intensify the storm. Comparing three TC experiments, it is clear that the area-averaged SST and enthalpy flux (latent heat flux plus sensible heat flux), as well as the intensity and intensification rate change with the TC translation speed. The largest intensity increase measured by the decrease in central pressure due to WCE is found in Trami (14 hPa), which has the slowest translation speed among the three simulated storms.

Figure 3.18 shows the spatial distributions of SST, OHC, and enthalpy flux to compare the WCE experiment with the CTRL experiment for Jebi on 0600 UTC 1 September. Results for Trami and Kong-rey are also shown in Figs 3.19 and 3.20, respectively. These figures are produced at the times of the maximum enthalpy flux differences between the WCE and CTRL experiments. The presence of the WCE significantly alters the SST response to TC. SST cooling is reduced in the presence of WCE as indicated by the SST anomaly calculated as WCE - CTRL (Figs 3.18c, 3.19c, and 3.20c). Figures 3.21, 3.22, and 3.23 show zonal vertical cross sections through the center of WCE for each TC to examine the evolution of the upper ocean thermal structure when the storm is passing over. The common feature noted in these cross sections is the TC-induced vertical mixing leads to a temperature decrease in the mixed layer and upper thermocline primarily to the right of the storm track. In the WCE experiments, however, the vertical mixing is suppressed by WCE compared to the CTRL experiment as indicated by the positive temperature differences in Figs 3.21c, 3.22c, and 3.23c. The presence of deep warm water with high OHC in the WCE serves as an insulator between the TC and cold ocean water below. This is in agreement with Lin et al. (2005) and other previous studies. The higher OHC values in the WCE, as seen in the OHC anomalies (Figs 3.18f, 3.19f, and 3.20f) inhibit upper ocean cooling underneath the storm, resulting in the increased enthalpy fluxes over the WCE (Figs 3.18i, 3.19i, and 3.20i). Maximum differences in area-averaged SST, OHC, and enthalpy fluxes within 100 km of the storm center and storm intensity between the CTRL and WCE experiments are summarized in Table 2. These differences are calculated during the period from the time when the storm enters the WCE area until one day after leaving the WCE. Although the same WCE is implemented at the same location for each experiment, the atmospheric and SST initial conditions created based on the real-time observational data vary depending on the initial time.

To compare the results and investigate the overall impacts of WCE, a maximum WCE potential index (MWPI) is introduced. MWPI compares the maximum differences between SST, HF, Pmin, Vmax in the uncoupled, coupled, and WCE experiments and is defined as

$$MWPI = \frac{\Delta I_{uncpl} - \Delta I_{WCE}}{\Delta I_{uncpl}} \times 100 \tag{2}$$

Where ΔI_{uncpl} is the maximum difference between the uncoupled and coupled experiments, and ΔI_{WCE} is the maximum difference between WCE and coupled experiments. Table 3 shows the average of maximum differences in SST, HF, Pmin, and Vmax between uncoupled and CTRL, and WCE and CTRL in four experiments for each storm, as well as MWPI. Overall, the largest maximum difference in SST and enthalpy flux is found in the Trami experiments. Accordingly, the maximum difference in storm intensity is also the largest in Trami cases. In WCE experiments for Trami, SST cooling is reduced by a maximum of 1°C due to the presence of WCE compared to the CTRL experiment. The reduced SST cooling and increased wind speed over the WCE lead to an increase of enthalpy flux by about 172 W/m^2. Consequently, Trami has the largest intensity increase of 10.75 hPa in minimum pressure and 9.9 m/s in maximum wind speed. It is interesting there are no significant differences in MWPI values between the storms. Overall, the MWPI varies from 23–31% for SST and HT, and 24–44% for Pmin. It is somewhat higher for Vmax, varying from 40–52%.

Additional sensitivity tests to the size of WCE on TC intensification are conducted. These experiments include WCE with the sizes of 140 km and 300 km, initialized on 0600 UTC 30 August for Jebi, 1200 UTC 23 September for Trami, and

1800 UTC 30 September for Kong-rey. The maximum different area-averaged values and storm intensity between the CTRL and different sizes of WCE experiments are summarized in Table 4. MWPI as a function of WCE size is shown in Fig 3.24. Overall, when the storm is interacting with a larger WCE a larger MWPI is found in SST and HF in all three storms. Consequently, the largest MWPI is found in the WCE experiments with 300 km, especially 77% of maximum potential wind speed for Jebi, and 64% and 63% for Trami and Kong-rey, respectively (Fig. 3.24d).

3.5 Conclusion

The impact of WCE on TC intensity is investigated in three tropical cyclones in the northwest Pacific. Four experiments have been performed for each TC to investigate the impact of WCE on storm intensification. To quantify the effect of WCE the area-averaged values within 100 km were calculated. Regardless of the storm translation speed, the presence of the WCE reduces the storm's self-induced upper ocean cooling and increases the latent heat flux for all storms, but the largest impact of WCE on SST response is found in Trami due to the slow translation speed. To investigate the maximum potential impact of WCE on ocean response and TC intensity, MWPI is calculated. For a WCE with a size of 200 km, the maximum WCE potential in reducing the SST cooling and increasing in heat fluxes ranges from 23–31% and decreasing in minimum pressure due to the presence of WCE ranges from 24–44%. The WCE effect is larger, 40–52%, for the maximum wind speed compared to the coupled cases with no WCE. MWPI increases to 63–77% for the maximum wind speed when the WCE size is increased to 300 km.

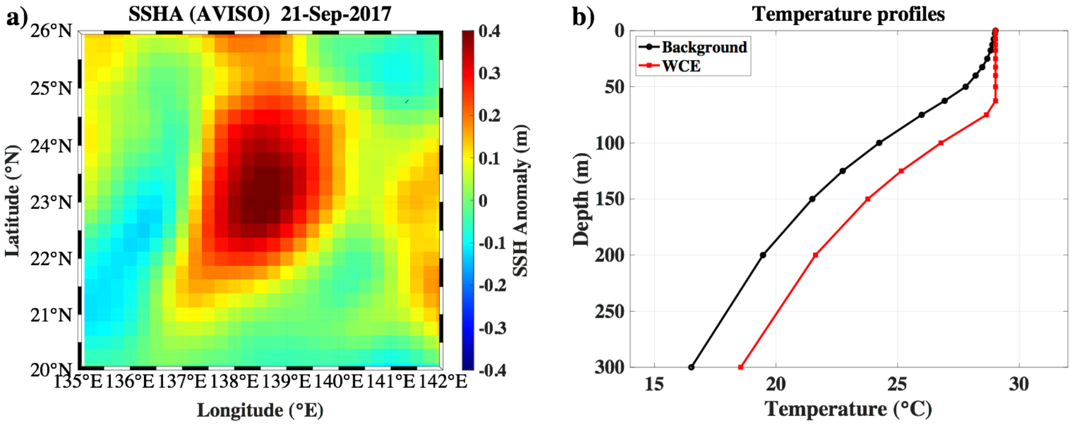

Figure 3.1. (a) Sea surface height anomaly (SSHA) in AVISO on 21 September 2017 and (b) temperature profiles in the background (black line) and center of WCE (red line) after adjustment according to Lin et al. (2005).

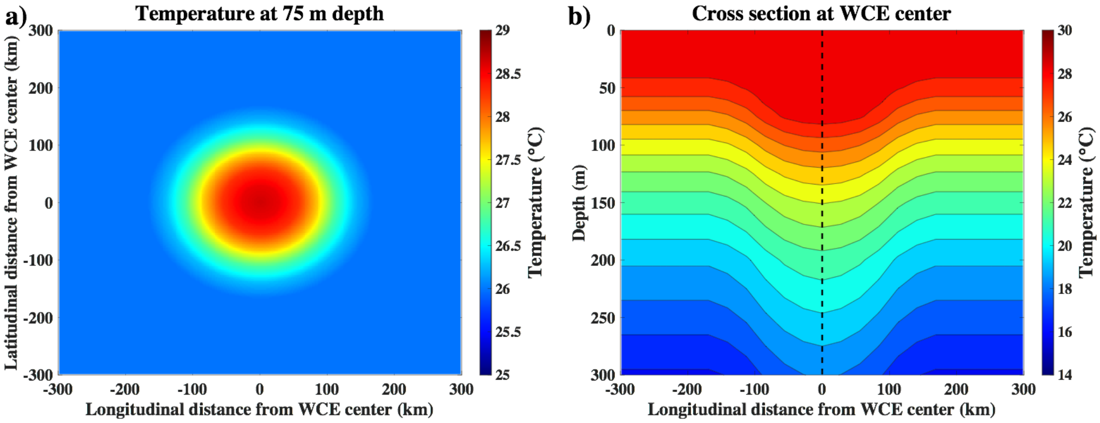

Figure 3.2. (a) Spatial distribution of 75 m ocean temperature (°C) in the idealized WCE and (b) zonal vertical cross section through the center of WCE. Vertical dashed line indicates the WCE center.

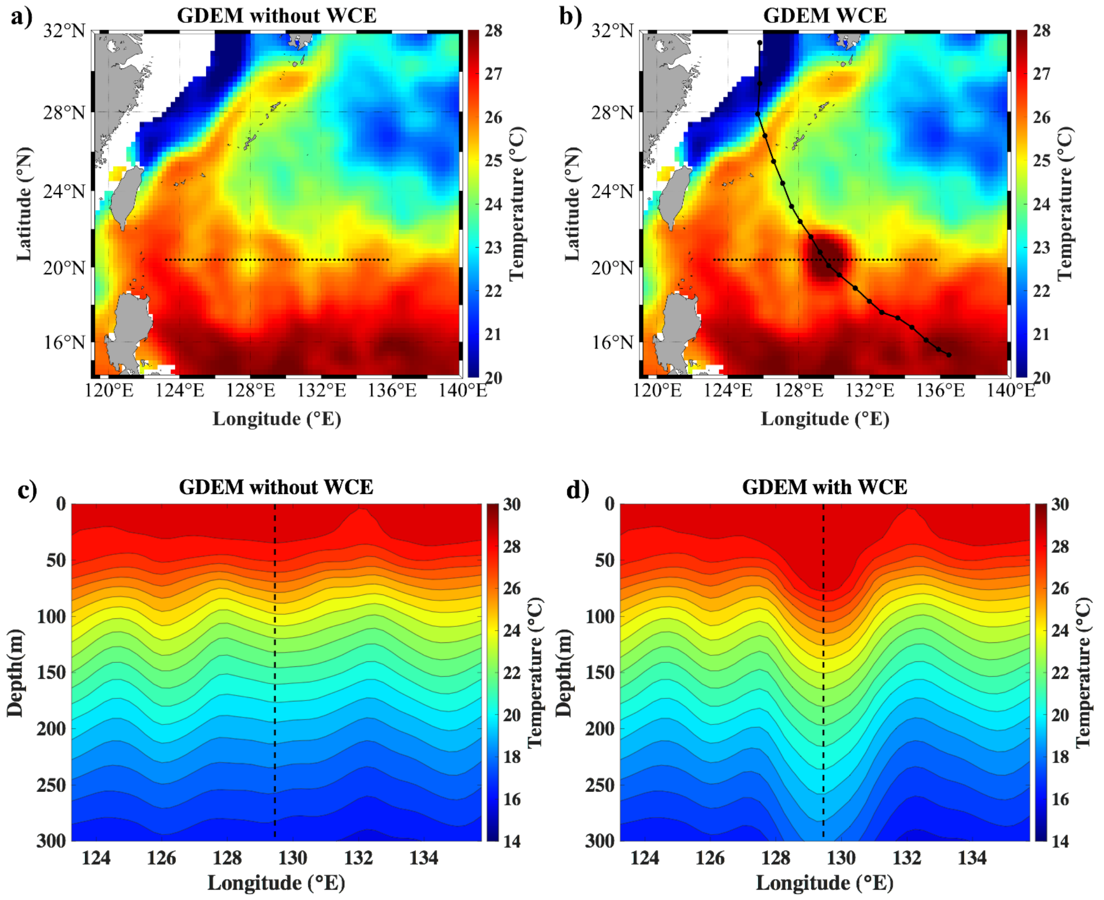

Figure 3.3. (a) Spatial distribution of 75 m ocean temperature (°C) in GDEM climatology and (c) zonal vertical cross section at 20.4°N along the dashed line in (a). (b) and (d) after WCE with 200 km assimilation into GDEM climatology for the TC Kong-rey experiment. Track and center positions of Kong-rey every 6 hours is overlaid in (b).

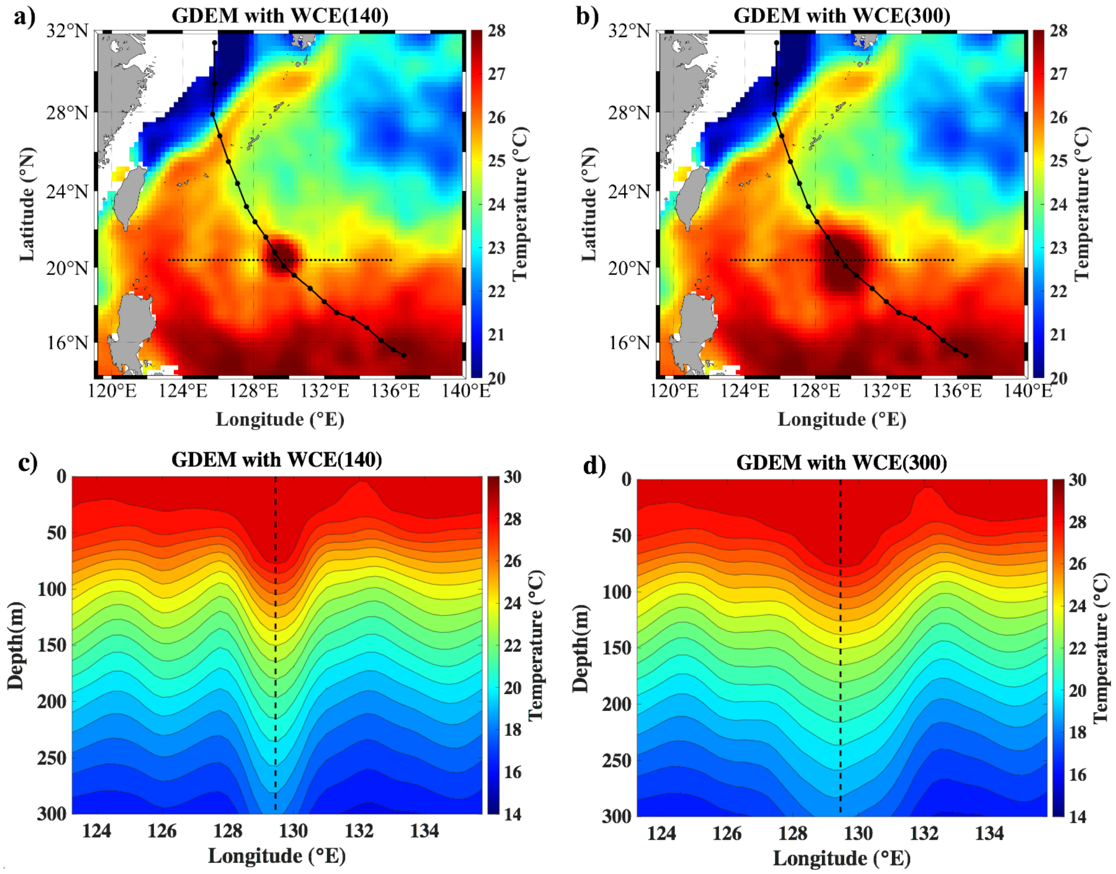

Figure 3.4. Same as fig. 3.3 for (a), (c) WCE with 140 km and (b), (d) WCE 300 km radius.

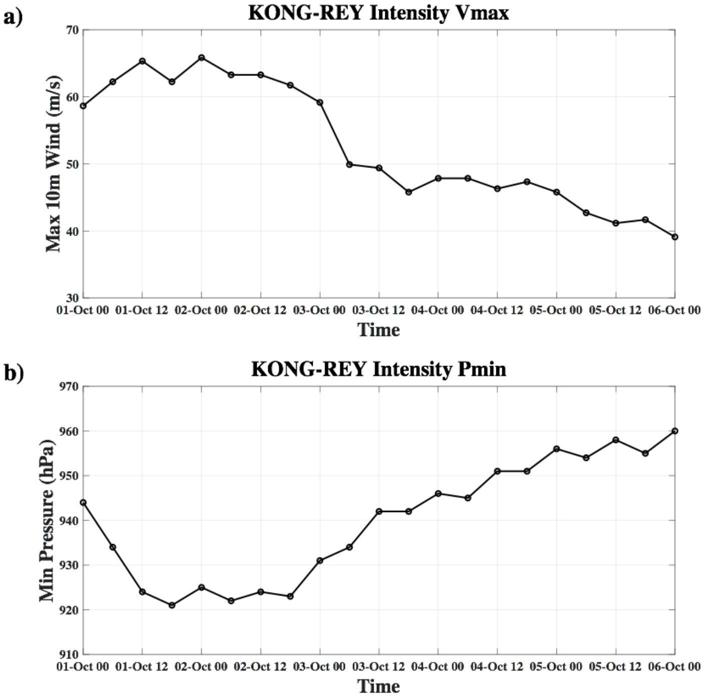

Figure 3.5. Time series of (a) maximum 10 m wind (m/s) and (b) minimum central pressure (hPa) evolution for Kong-rey CTRL experiment.

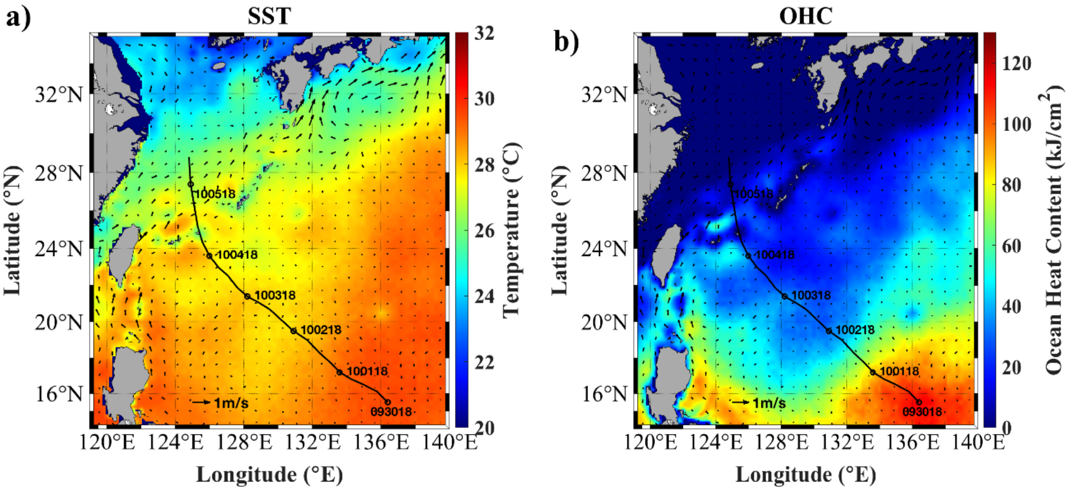

Figure 3.6. Spatial distribution of (a) SST and (b) OHC with ocean currents at 1800 UTC 30 September. Track of Kong-rey from the model is shown in black line with the storm center position (circles) at the time shown.

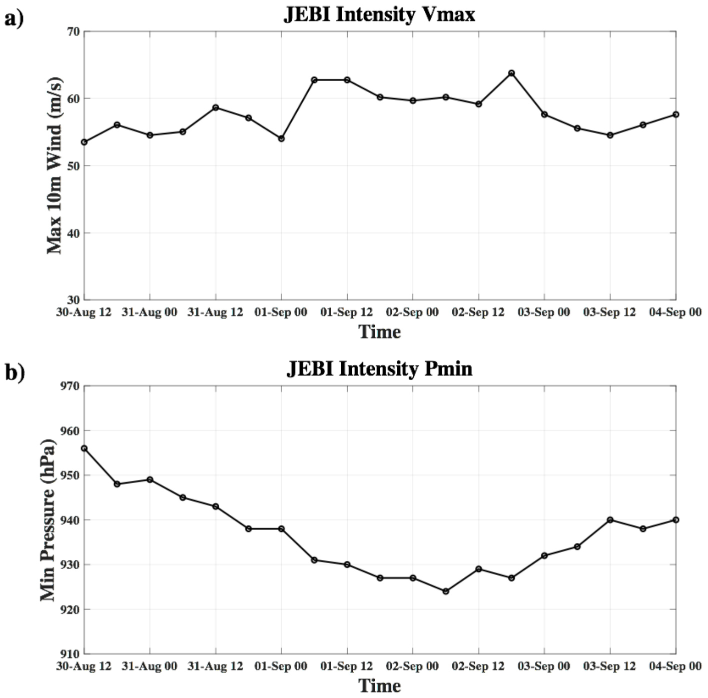

Figure 3.7. Same as fig. 3.5 for Jebi CTRL experiment.

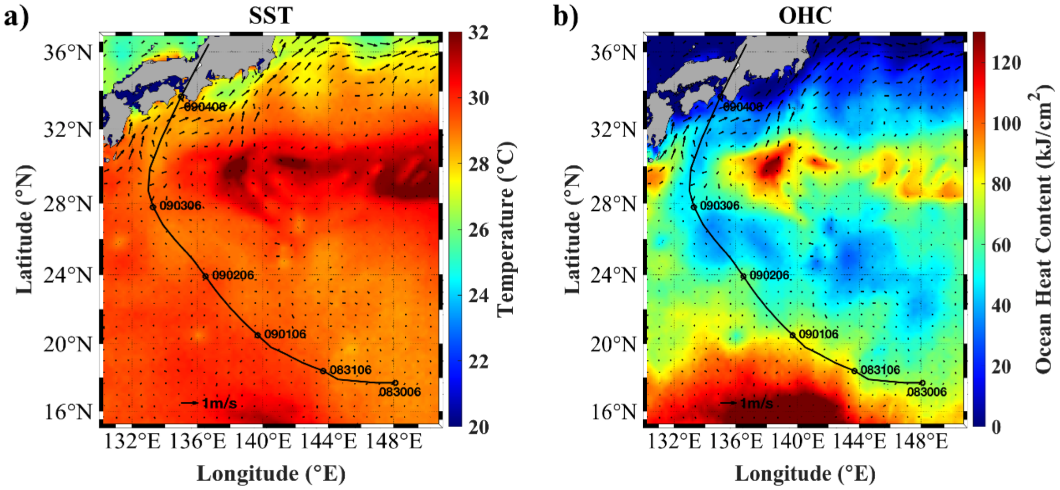

Figure 3.8. Spatial distribution of (a) SST and (b) OHC with ocean currents at 0600 UTC 30 August. Track of Jebi from the model is shown in black line with the storm center position (circles) at the time shown.

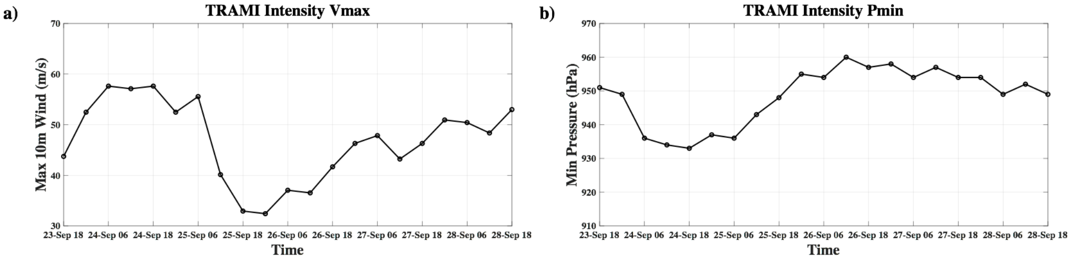

Figure 3.9. Same as fig. 3.5 for Trami CTRL experiment.

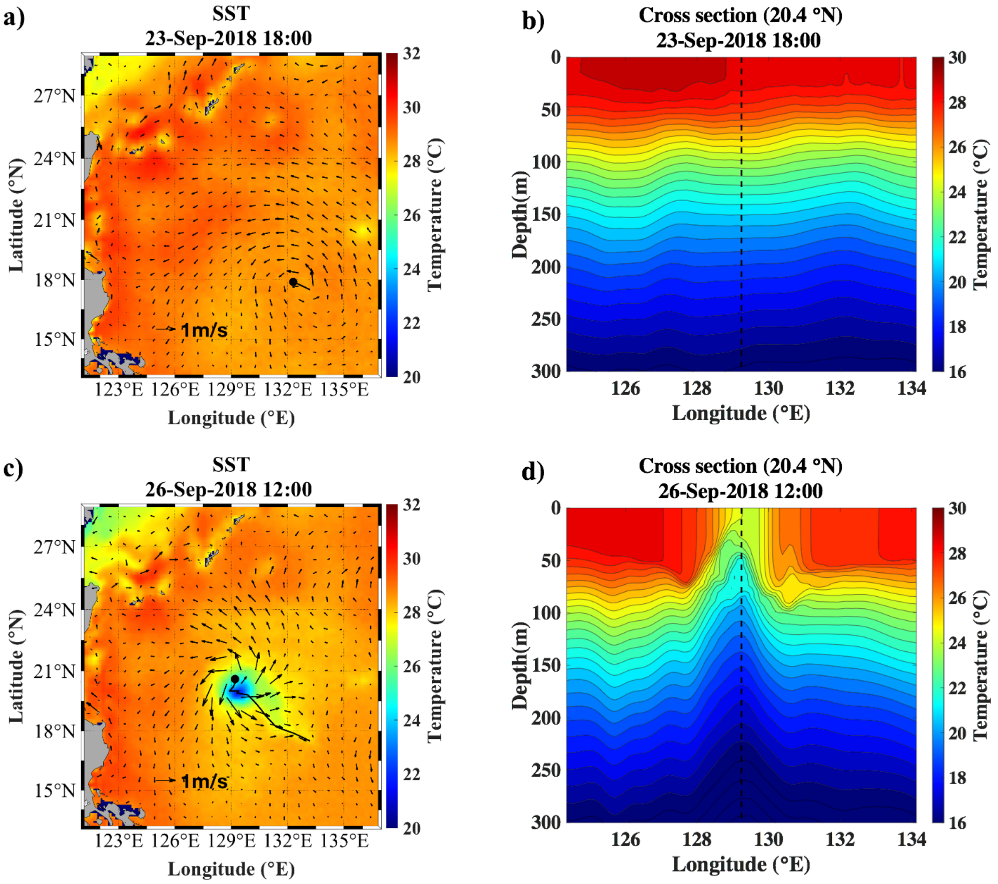

Figure 3.10. (a) Spatial distribution of SST with ocean currents at 1800 UTC 23 September and (c) at 1200 UTC 26 September. (b) Zonal cross section at 20.4°N at 1800 UTC 23 September and (d) at 1200 UTC 26 September.

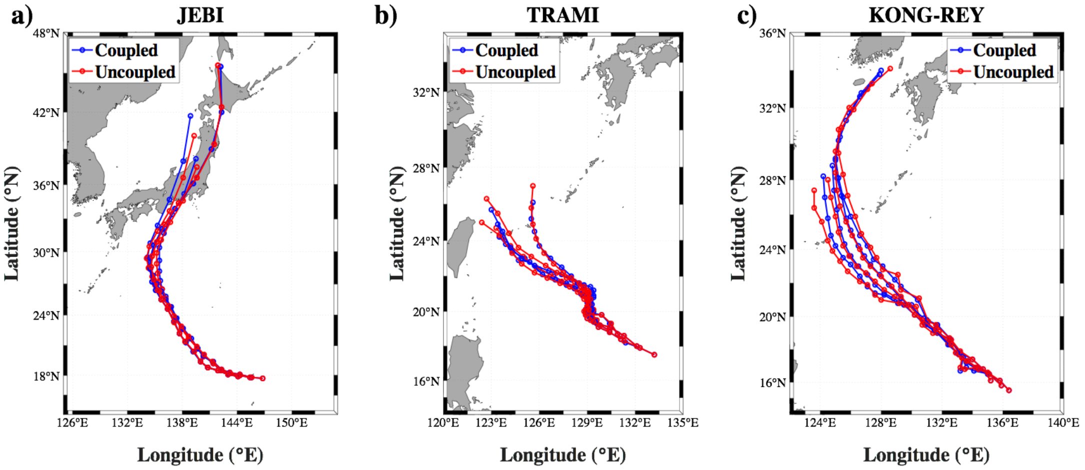

Figure 3.11. Model Tracks of coupled (blue) and uncoupled (red) experiments for (a) Jebi, (b) Trami, and (c) Kong-rey. Circle along the tracks indicates the storm center every 6 hours.

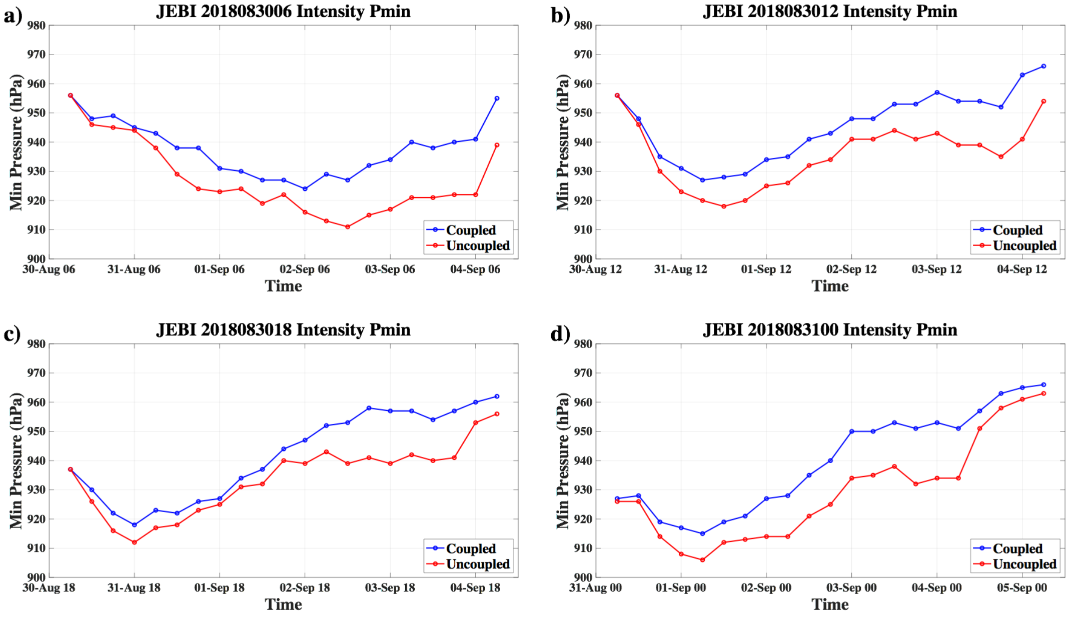

Figure 3.12. Time series of minimum central pressure (hPa) of coupled (blue) and uncoupled (red) experiments for Jebi.

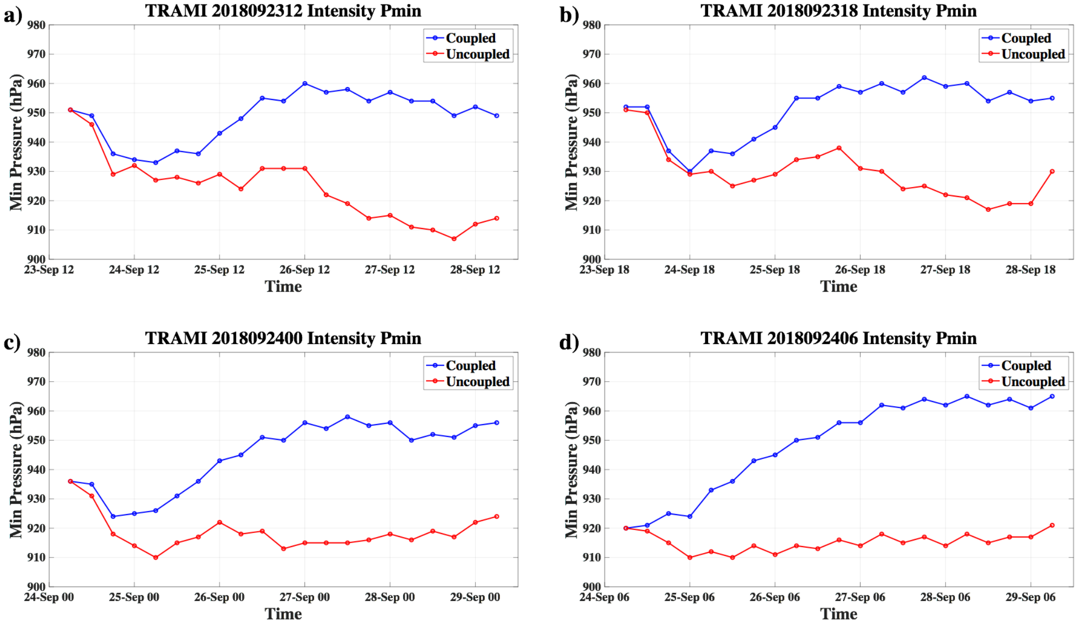

Figure 3.13. Same as fig. 3.12 for Trami.

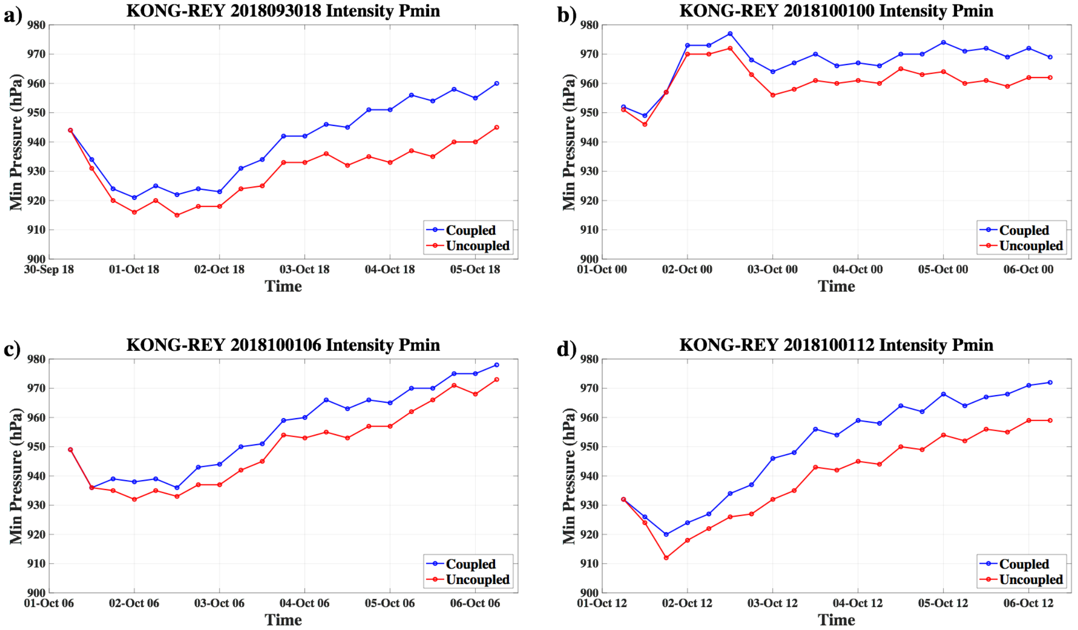

Figure 3.14. Same as fig. 3.12 for Kong-rey.

Table 1. Maximum different values between uncoupled and
CTRL experiments in different initial times.

JEBI	0600 30 Aug	1200 30 Aug	1800 30 Aug	0000 31 Aug
ΔSST (℃)	1.20	1.52	1.52	1.41
ΔHF (W/m^2)	340.23	237.04	262.52	304.84
ΔPmin (hPa)	19	15	18	19
ΔVmax (m/s)	13.38	11.83	11.83	19.03

TRAMI	1200 23 Sep	1800 23 Sep	0000 24 Sep	0600 24 Sep
ΔSST (℃)	3.75	2.95	3.70	3.77
ΔHF (W/m^2)	719.57	679.87	729.01	792.11
ΔPmin (hPa)	44	39	43	48
ΔVmax (m/s)	23.15	23.66	22.64	30.35

KONG-REY	1800 30 Sep	0000 1 Oct	0600 1 Oct	1200 1 Oct
ΔSST (℃)	1.69	1.42	2.06	2.53
ΔHF (W/m^2)	333.42	312.06	105.62	193.24
ΔPmin (hPa)	19	11	11	14
ΔVmax (m/s)	15.43	16.98	6.69	15.95

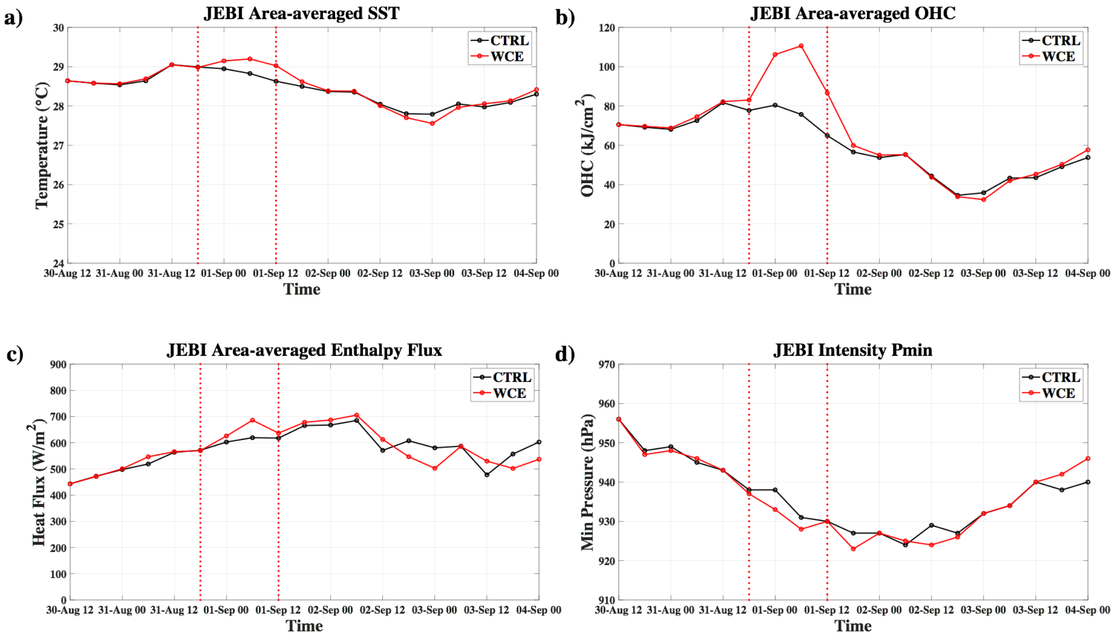

Figure 3.15. Time series of area-averaged (a) SST, (b) OHC, (c) enthalpy flux within 100 km radius, and (d) minimum central pressure (hPa) for Jebi. Vertical red dashed lines indicate the time when the storm is passing over WCE.

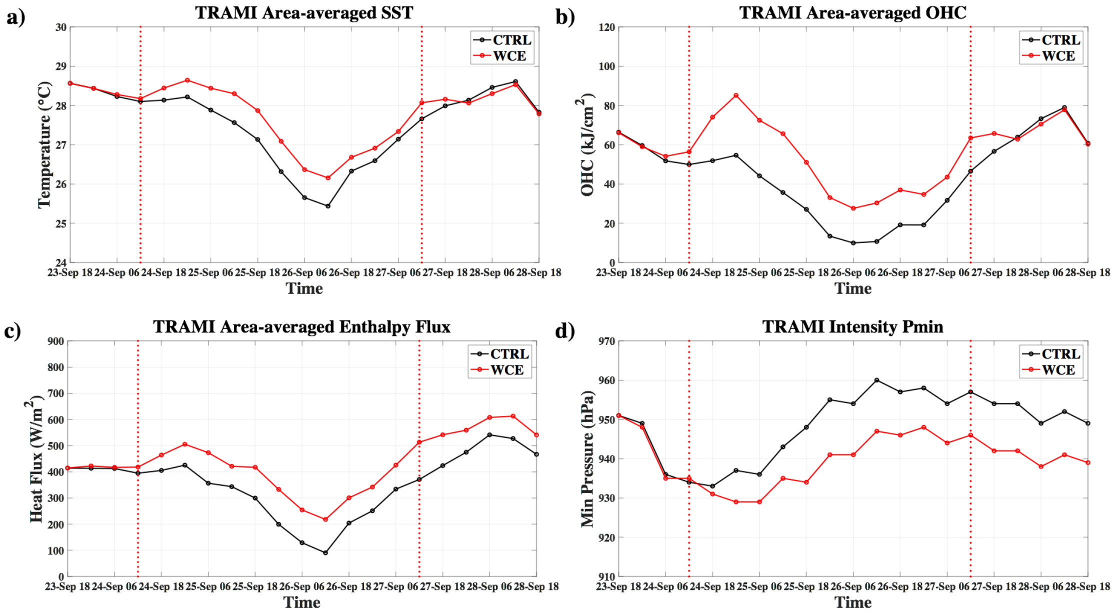

Figure 3.16. Same as fig. 3.15 for Trami.

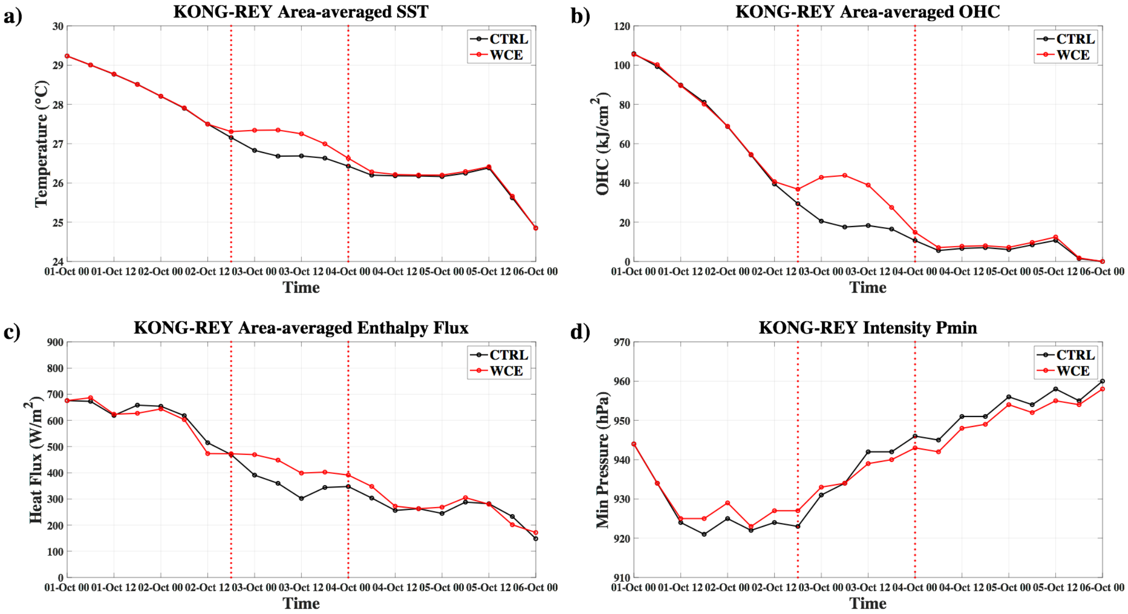

Figure 3.17. Same as fig. 3.15 for Kong-rey.

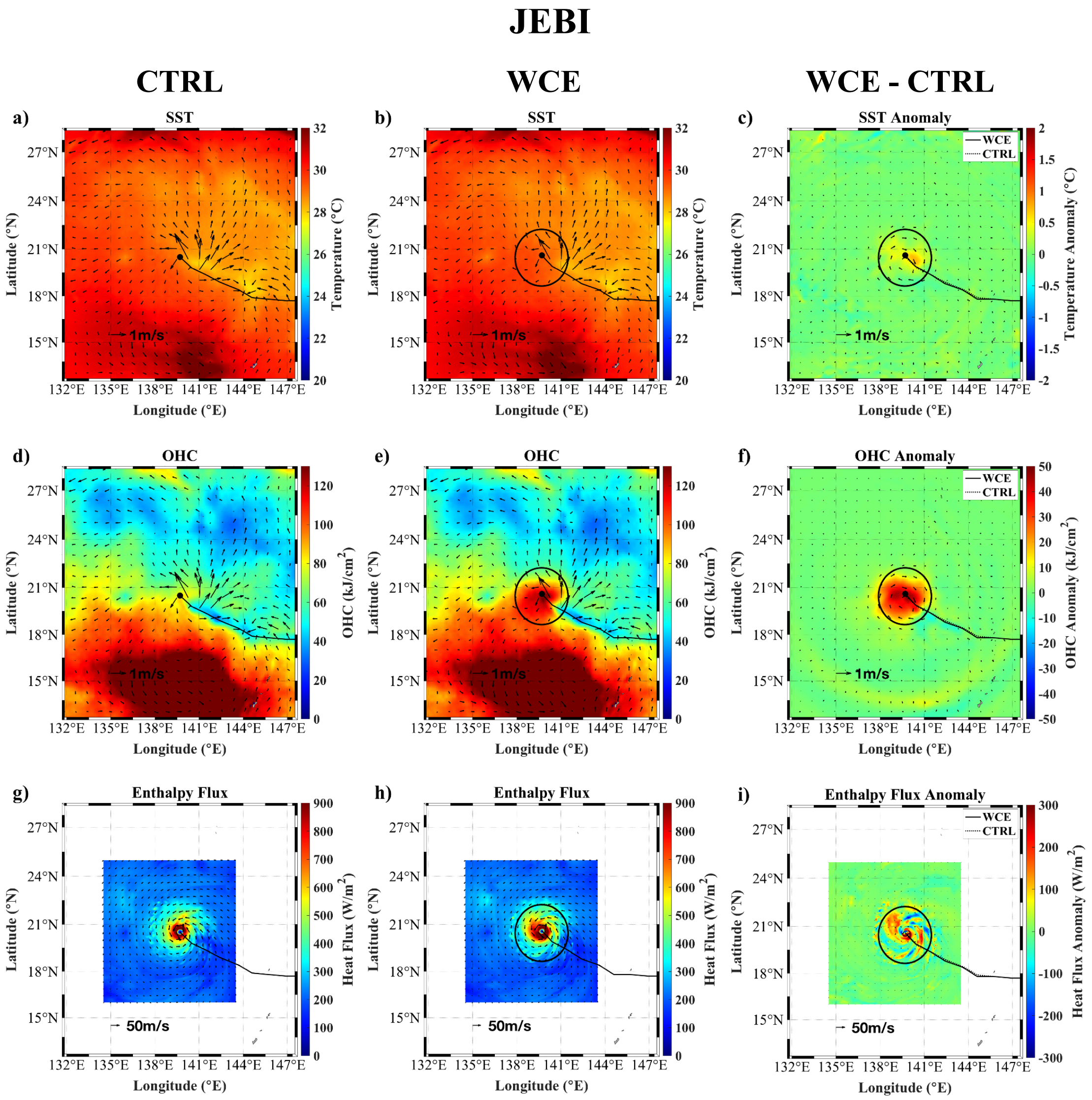

Figure 3.18. Spatial distribution of (a), (b) SST and (c) anomaly, and (d), (e) OHC and (f) anomaly, and (g), (h) enthalpy flux and (i) anomaly responded by Jebi at 0600 UTC 1 September, where the anomaly is calculated as WCE - CTRL. Black circle indicates the location and approximate size of WCE, and black dot indicates the storm center. Solid and dashed lines in anomalies indicate track of WCE and CTRL experiments, respectively.

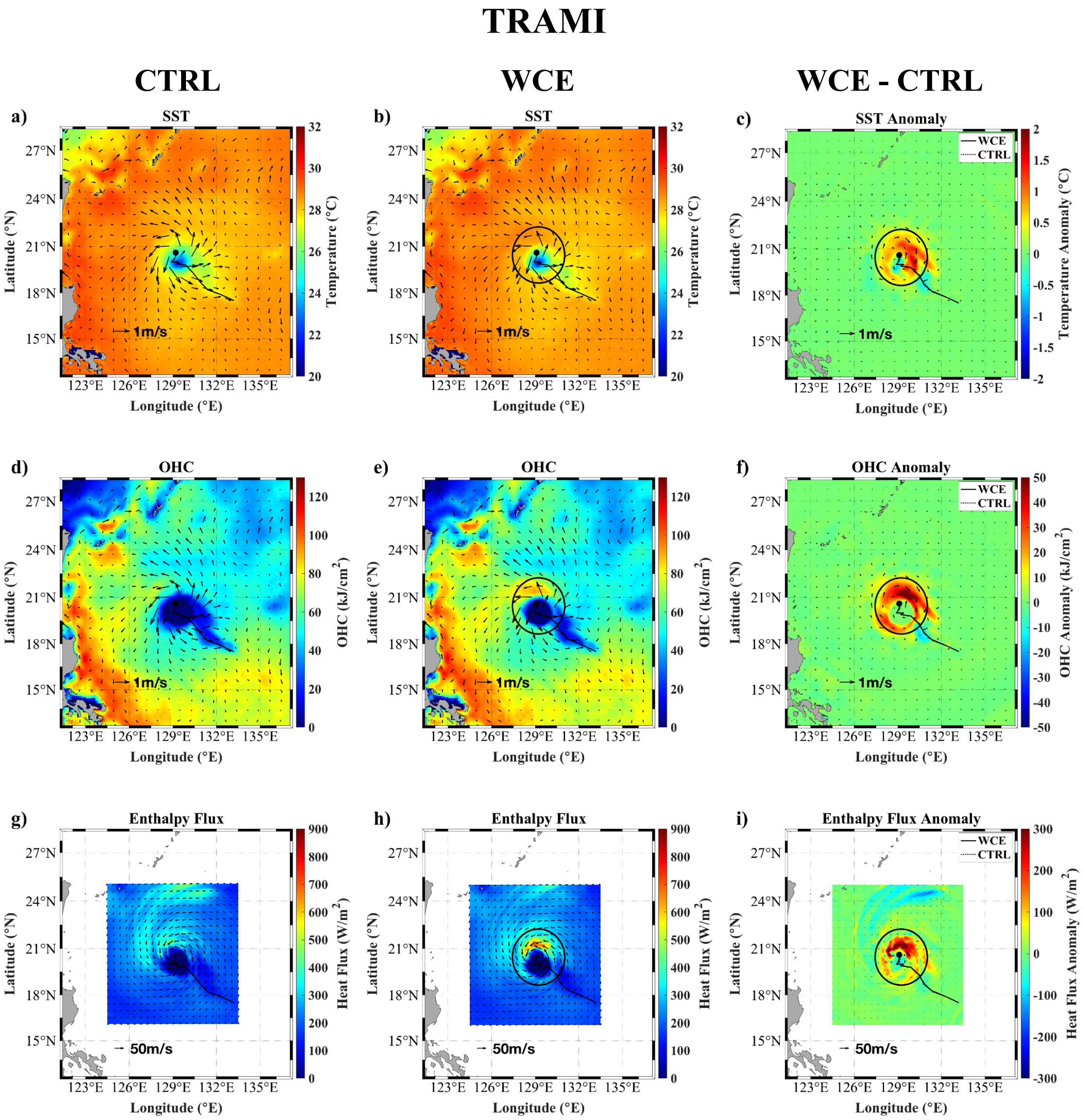

Figure 3.19. Same as fig. 3.18 for Trami at 1200 UTC 26 September.

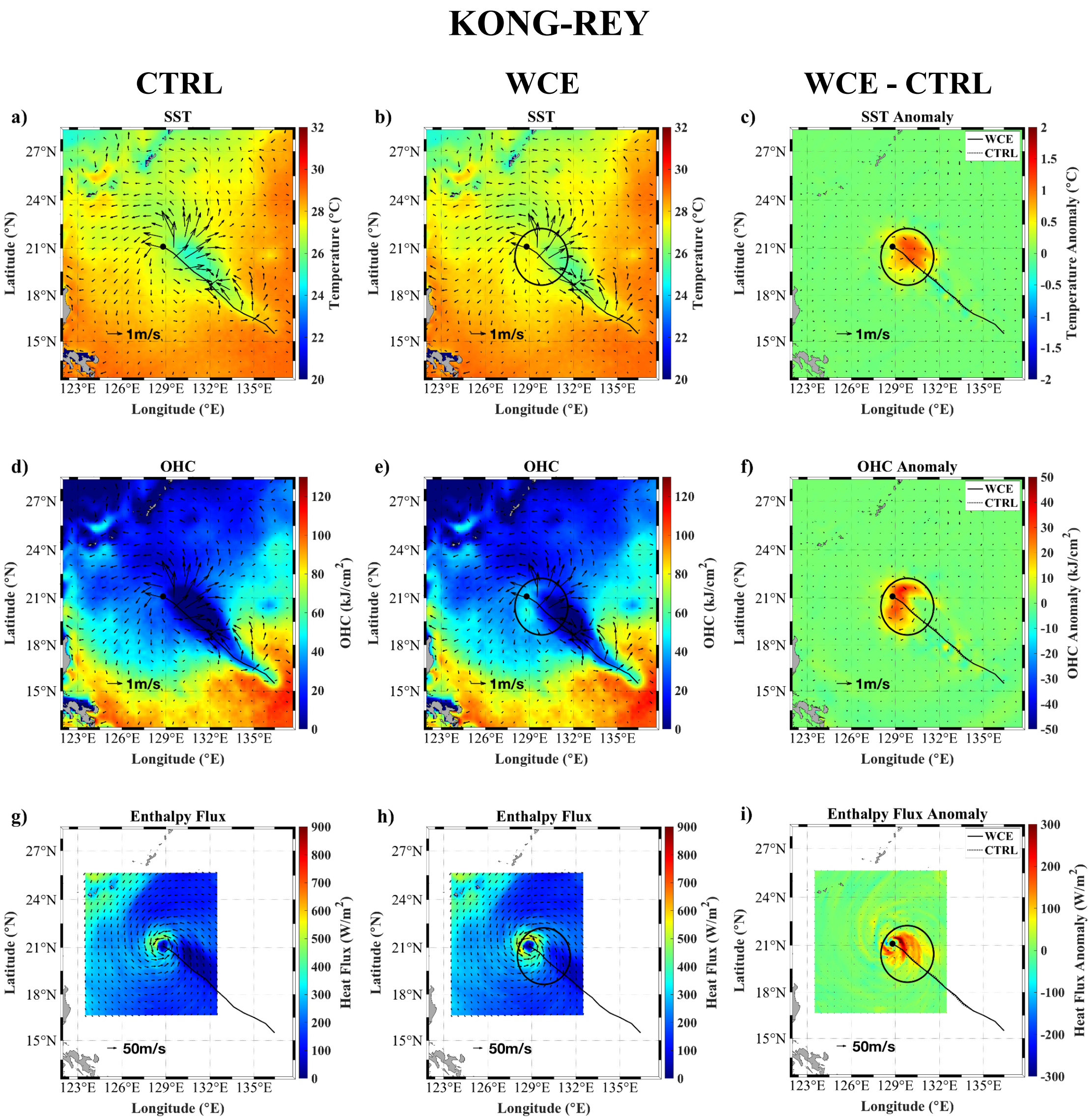

Figure 3.20. Same as fig. 3.18 for Kong-rey at 1200 UTC 3 October.

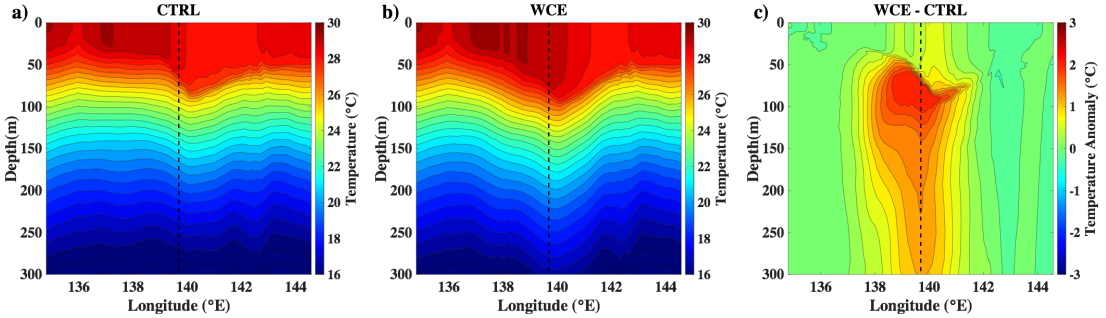

Figure 3.21. Zonal vertical cross section at the center of WCE (20.4°N) in (a) CTRL, (b) WCE and (c) WCE - CTRL for Jebi at 0600 UTC 1 September. Vertical dashed line indicates the center of WCE.

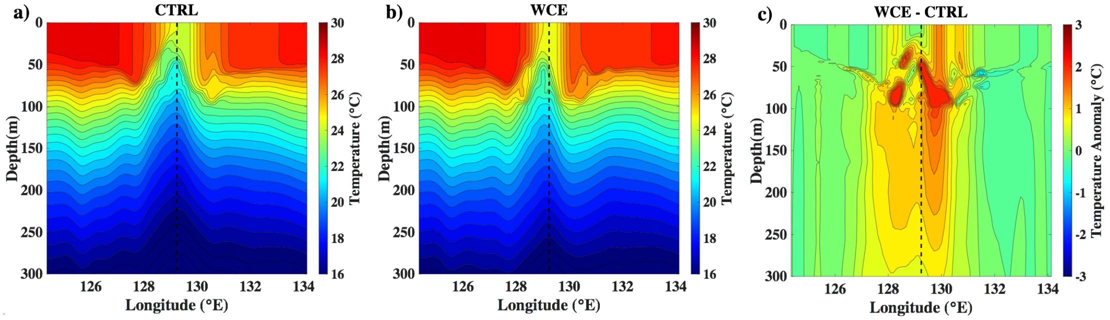

Figure 3.22. Same as fig 3.21 for Trami at 1200 UTC 26 September.

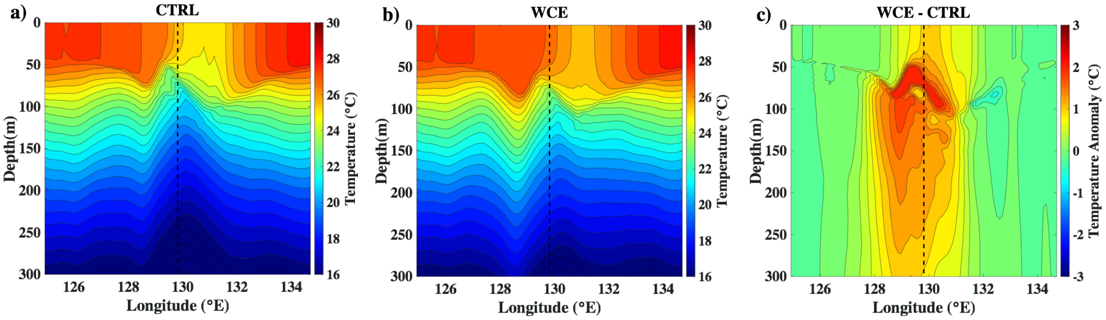

Figure 3.23. Same as fig. 3.23 for Kong-rey at 1200 UTC 3 October.

Table 2. Maximum different values between WCE (200) and CTRL experiments in different initial times.

JEBI	0600 30 Aug	1200 30 Aug	1800 30 Aug	0000 31 Aug
ΔSST (℃)	0.40	0.42	0.37	0.44
ΔOHC (kJ/cm^2)	34.88	27.99	25.22	33.16
ΔHF (W/m^2)	66.77	110.04	52.51	90.99
ΔPmin (hPa)	5	7	1	5
ΔVmax (m/s)	8.23	7.72	3.60	5.14

TRAMI	1200 23 Sep	1800 23 Sep	0000 24 Sep	0600 24 Sep
ΔSST (℃)	0.77	1.02	1.10	1.12
ΔOHC (kJ/cm^2)	30.52	29.90	26.68	25.01
ΔHF (W/m^2)	142.57	206.94	183.17	156.24
ΔPmin (hPa)	14	10	11	8
ΔVmax (m/s)	11.32	8.75	9.26	10.29

KONG-REY	1800 30 Sep	0000 1 Oct	0600 1 Oct	1200 1 Oct
ΔSST (℃)	0.66	0.33	0.38	0.44
ΔOHC (kJ/cm^2)	26.30	21.73	22.75	23.49
ΔHF (W/m^2)	96.80	35.11	46.60	76.96
ΔPmin (hPa)	3	9	4	6
ΔVmax (m/s)	5.66	13.38	4.63	3.60

Table 3. Average values and MWPI of four
initial time experiments in table 1 and 2.

JEBI				
	ΔSST (°C)	ΔHF (W/m^2)	ΔPmin (hPa)	ΔVmax (m/s)
ΔI_{WCE}	0.41	80.08	4.50	6.17
ΔI_{uncpl}	1.41	286.16	17.75	14.02
MWPI	29.1%	29%	26.2%	46.1%

TRAMI				
	ΔSST (°C)	ΔHF (W/m^2)	ΔPmin (hPa)	ΔVmax (m/s)
ΔI_{WCE}	1.00	172.23	10.75	9.90
ΔI_{uncpl}	3.54	730.14	43.5	24.95
MWPI	28.6%	23.8%	24.9%	40.2%

KONG-REY				
	ΔSST (°C)	ΔHF (W/m^2)	ΔPmin (hPa)	ΔVmax (m/s)
ΔI_{WCE}	0.45	63.87	5.50	6.82
ΔI_{uncpl}	1.93	236.09	13.75	13.76
MWPI	24.5%	31.1%	44.2%	51.8%

Table 4. Maximum different values between
different sizes of WCE and CTRL experiments.

JEBI	WCE (140)	WCE (200)	WCE (300)
ΔSST (°C)	0.31	0.40	0.42
ΔOHC (kJ/cm^2)	25.84	34.88	42.88
ΔHF (W/m^2)	31.20	66.77	100.53
ΔPmin (hPa)	3	5	5
ΔVmax (m/s)	4.12	8.23	10.29

TRAMI	WCE (140)	WCE (200)	WCE (300)
ΔSST (°C)	0.80	0.77	0.97
ΔOHC (kJ/cm^2)	20.90	30.52	35.55
ΔHF (W/m^2)	133.91	142.57	206.55
ΔPmin (hPa)	12	14	13
ΔVmax (m/s)	11.32	11.32	14.92

KONG-REY	WCE (140)	WCE (200)	WCE (300)
ΔSST (°C)	0.50	0.66	0.73
ΔOHC (kJ/cm^2)	18.50	26.30	30.30
ΔHF (W/m^2)	79.22	96.80	156.85
ΔPmin (hPa)	2	3	9
ΔVmax (m/s)	7.72	5.66	9.77

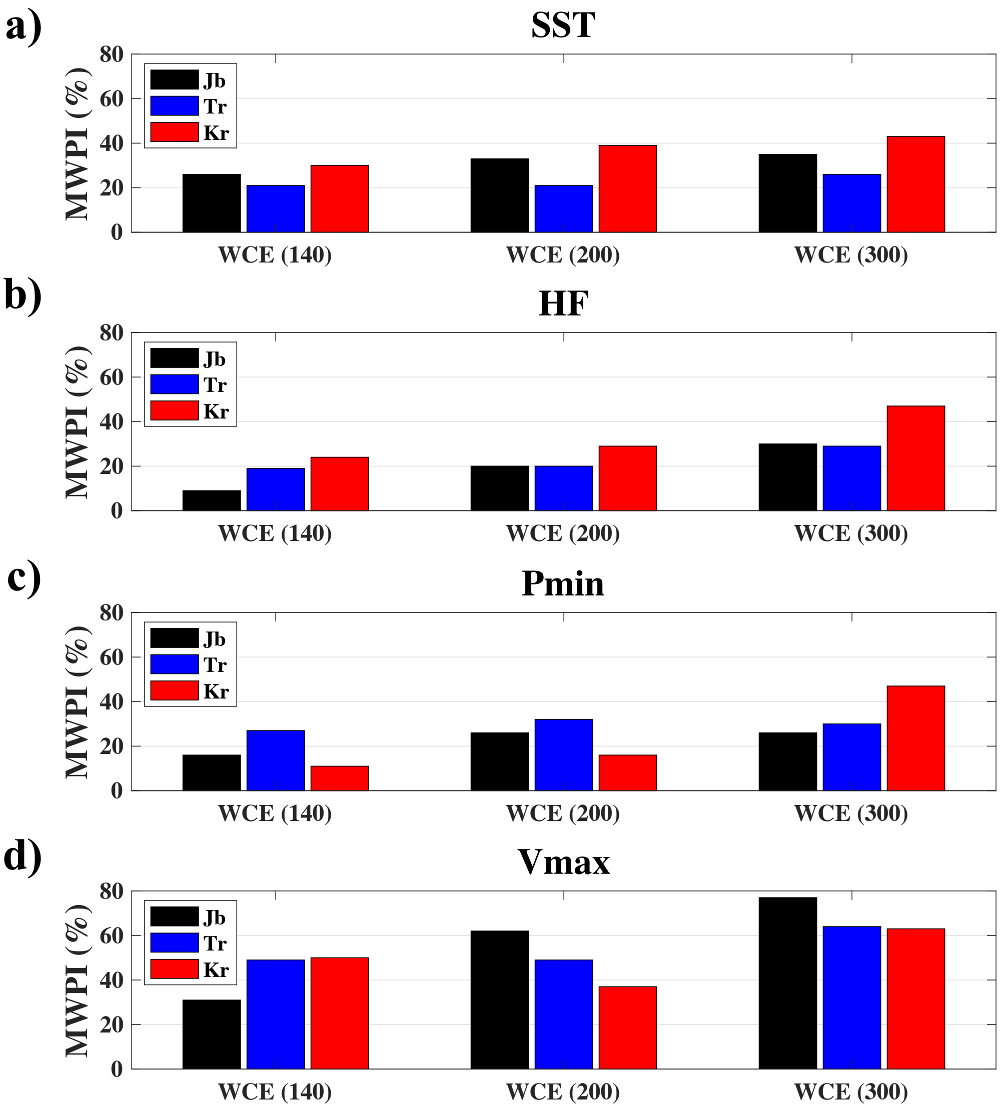

Figure 3.24. MWPI of (a) SST, (b) HF, (c) minimum pressure, and (d) maximum wind speed for Jebi (black), Trami (blue), and Kong-rey (red) as a function of WCE size (radius; unit: km). Initial time for Jebi is 0600 UTC 30 August, Trami is 1200 UTC 23 September, and Kong-rey is 1800 UTC 30 September.

Chapter 4

Impact of Oceanic Barrier Layers on TC Intensity

4.1 Initialization and Experiment Design

There are regions where low-salinity water is located near the surface, and these low-salinity layers can induce barrier layers (BLs) when the isothermal layer depth (ILD) is deeper than the mixed layer depth (MLD). Figure 4.2 shows the schematic temperature, salinity, and density profiles to show barrier layer thickness (BLT). BLT is defined as the difference in the isothermal (ILD) and mixed layer depth (MLD). ILD is defined as the level at which the temperature deviates from reference depth of 10 m temperature by ΔT= 0.2°C, and MLD is defined as the depth at which the potential density σ exceeds the σ at 10 m by the same amount that it would for a temperature decrease of the same ΔT for a constant salinity (de Boyer Montegut et al., 2007).

$$\Delta\sigma = \sigma(T - \Delta T, S, P) - \sigma(T, S, P). \tag{3}$$

The contribution of low-salinity water in the upper ocean to storm intensification was observed during the KIOST field experiment in 2019. TC Lingling rapidly intensified from a weak category 1 at UTC 00:00 4 September to category 4 over 24 hours while passing along the western side of WCE (Fig. 4.1) (Kang et al., 2020). Vertical temperature and salinity cross section at each CTD casting along the section E of WCE before and after Lingling passage are shown in Fig 4.1. The high temperature of 28–29.5˚C and relative lower salinity of 34.4–34.5 psu in the western side of WCE before Lingling passage suggest that the low salinity water is wrapping around the west of WCE (Figs 4.1b and 4.1c). It is suggested that the weak cooling of less than 0.5˚C occurred due to the low salinity water, which served as the barrier layer, led to the rapid intensification of Lingling (Figs 4.1d and 4.1e).

We conducted simulations to explore the effect of BL on three TCs in 2018, Jebi, Trami, and Kong-rey in the northwest Pacific. Each simulation is initialized using one temperature and one of four different salinity profiles indicating different BLT. Figure 4.3 shows the temperature, salinity, and density profiles used in the idealized experiments based on Hlywiak and Nolan (2019). These temperature, salinity, and BLT are consistent with the observations in the Amazon–Orinoco plume region, but the BL with similar characteristics is found in the western Pacific or the Bay of Bengal (Neetu et al., 2012; Yan et al., 2017). The three BL cases have BLT of 15, 20, and 25 m, and the initial sea surface salinity values for each are 35.39 (OBL15), 33.84 (OBL20), and 31.32 (OBL25) psu. The list of BL experiments is shown in Table 5. In every simulation, the initial temperature is constant down to the ILD at 50 m depth.

4.2 Impact of Barrier Layer on TC intensity

Previous studies found that the SST response to a passing TC depends on the ocean thermal structure, and TC conditions such as its size, intensity, and translation speed (Price 1983; Shay et al., 1989; Yablonsky and Ginis, 2009). To investigate the impact of the BL on TC intensity, which is expected to be a favorable ocean condition for storm intensification, it is important to examine different TC conditions because the upper ocean response is strongly influenced by the TC intensity and translation speed. Figure 4.4 shows the time series of the area-averaged SST cooling and SST anomaly relative to OBL00 for each OBL case within 100 km of the storm center for each storm. The total simulation time is 96 h for each experiment and the result is provided every 6 hours. Before discussing the impact of BLT, it is important to examine first the sea surface cooling trend due to the different characteristics of each storm. Overall, the magnitude of SST cooling is larger for the slower moving storm (Figs 4.4a, 4.4c, and 4.4e). Unlike the gradual increase in SST cooling trends in TC Kong-rey and Jebi, rapid cooling occurs in TC Trami from the time at 0600 UTC 25 September as the translation speed slows down (Fig. 2.5). The peak of the cooling is reached at 1200 UTC 26 September after which the cooling is reduced due to do acceleration of the translation speed and storm weakening (Fig 4.4c).

In all experiments, TC-induced cooling has been suppressed by the presence of BL, especially in OBL20 and OBL25 cases. The maximum cooling difference is found in the OBL20 case in Trami, by about 0.7℃ compared to the OBL00 case, and in OBL25 cases for Kong-rey and Jebi, by over 0.4℃ and 0.2℃, respectively (Figs 4.4b, 4.4d, and 4.4f). These results indicate that the effect of BL on the SST response is highly dependent on the TC translation speed. This is in agreement with idealized TC simulations by Hlywiak and Nolan (2019). An interesting result is found that the reduced cooling due to the presence of the BL occurs from the beginning of the simulation in the Kong-rey experiments (Fig. 4.4f). In contrast, there is a little cooling difference at the beginning of the Jebi experiments and it becomes noticeable at 0000 UTC 1 September, 42 h after the simulation begins. To explain this result, the azimuthally averaged wind speed is calculated from the storm center in the OBL25 and OBL00 experiments in Jebi, Trami, and Kong-rey (Fig 4.5). In Kong-rey, the maximum averaged wind speed is found further from the storm center compared to Jebi and Trami. This implies that a larger area in the ocean is affected by the strong wind under Kong-rey, which can explain why the impact of BL in reducing SST cooling due to the BL occurs earlier in the Kong-rey case.

Spatial distribution of SST anomaly between OBL25 and OBL00 cases for three TCs is shown in Fig. 4.6. After 24 h of simulation SSTs behind the TC center are warmer since the surface cooling is inhibited due to the BL for all TC OBL25 cases. However, after 60 h of simulation the increased SST cooling is found along the track behind in Jebi and Kong-rey. The increased cooling is located further from the storm center in Jebi and closer to the storm center in Kong-rey. The increased cooling is due to increased upwelling generated by the current divergence along the TC track in the BL experiments. Upwelling along the storm track brings the cold water from the thermocline closer to the ocean surface (Price 1981). The increased upwelling in the presence of BL can be explained as follows. TC wind-induced upper ocean mixing is reduced due to BL which leads to stronger surface current and thus stronger current divergence along the TC track. Distance from the TC center to the location of maximum upwelling can be estimated as

$$U_h(\pi - \alpha)/f \tag{4}$$

where U_h is the storm translation speed and α is the inflow angle (the angle between the wind vector and the azimuthal direction) and f is Coriolis parameter (Ginis 2002). In the case of TC Jebi, the maximum upwelling occurs further from the center than in Kong-rey because Jebi’s translation speed is higher. As a result, the BL induced SST cooling is found at a larger distance in Jebi compared to Kong-rey (Fig. 4.6b and Fig. 4.6f). After the 24 hours of the Trami simulation, SST cooling is reduced due the BL (Fig. 4.6c), however, after 60 h SST field shows greater cooling near the storm center.

This is because upwelling occurs closer to the center due to Trami's slow translations speed. In this case, the BL is completely eroded by mixing and upwelling, and the upper ocean is well mixed with the subsurface layer underneath the TC. The upper ocean mixing is seen in the vertical cross section in Fig. 4.7. At the beginning of the simulation, the cooling in the mixed layer is reduced because of the BL (Fig. 4.7e). Nevertheless, the increased cooling due to the BL is found after 60 h of simulation at the right of the storm center around 130°E and left around 128°E (Fig. 4.7f). This demonstrates that the presence of BL contributes to the reduced upper ocean mixing beneath the TC but also to increase the upwelling generated by the divergent ocean surface currents.

Figure 4.8 shows the time series of area-averaged enthalpy flux evolution within 100 km. In Kong-rey, the enthalpy fluxes in OBL20 and OBL25 cases increase at the beginning of the simulation due to the early decreased SST cooling. Noticeably, changes in the enthalpy flux are smaller in Trami than in the other TCs. The time series of the minimum central pressure evolution are shown in Fig. 4.9 to investigate the impact of BL on storm intensity. The storm intensification owing to BL occurs in all TC cases, and the larger difference is found in OBL20 and OBL25 cases (Figs 4.9b, 4.9d, and 4.9f). The results of Trami do not support the Hlywiak and Nolan (2019) conclusion that there was a greater impact of BL on TC intensity for slower-moving storms. It is because the Trami has two features, the slow translation speed and changing the direction of storm movement when it slows down. Both allow Trami to have enough time to generate the vertical mixing as well as the upwelling over the same region, so the impact of the BL on Trami is comparable to that in Jebi and Kong-rey.

The maximum area-averaged values of SST and HF within 100 km of the storm center, as well as storm intensity (Pmin and Vmax) between the OBLx and OBL00 experiments are summarized in Table 6. In all the experiments, the presence of BL lead to reduction of SST cooling and increased heat fluxes which lead to an increase of TC intensity. Overall, the largest intensity differences are found in the OBL20 and OBL25 cases as expected due to larger BLT. However, no direct correlation between the SST and HF changes and TC intensity can be identified. In Jebi, increasing BLT leads to an increase in the maximum difference of SST and enthalpy flux. However, Trami and Kong-rey have the largest enthalpy flux difference due to BL in OBL20 cases, and the largest intensity differences are not consistently found in minimum pressure and maximum wind speed. Comparing the maximum difference values may not be the best indication of the impact of the BL on intensity in real TCs.

4.3 Conclusion

The influence of BL on TC development is investigated in three real tropical cyclones in the northwest Pacific. In our results, the presence of the BL has an effect on the upper ocean response by reducing the entrainment of colder water below into the sea surface and thus increasing the intensity of the storm. This finding agrees with idealized coupled model results in Hlywiak and Nolan (2019) and other previous studies. In the BL experiments, the maximum increased intensity is around 6 to 9 hPa compared to the CTRL experiments. However, we have inconsistent results in sensitivity tests to storm translation speed and oceanic barrier layer thickness. Hlywiak and Nolan (2019) found that the degree of the barrier layer favorable effect on TC intensification increases with increasing the BL thickness and increases for decreasing translation speed. We find maximum increased intensity in minimum pressure in the

OBL25 cases for Jebi (fast moving TC) and Trami (slow moving TC). Nevertheless, the impact on TC intensity was the largest in OBL20 for Kong-rey. Besides, the impact of BL on the intensity of Trami is not greater compared to that of other TCs. Since the three TCs used in this study are the real storms occurring in 2018 the results are more complicated than using the idealized background wind. Additionally, it is found that the BL may increase the magnitude of upwelling along the storm track depending on the TC translation speed. Our results show that the enhanced upwelling in slow moving TCs can increase SST cooling underneath the storm and thus compensate for the SST cooling decrease due to the BL. This effect needs to be examined further in future studies.

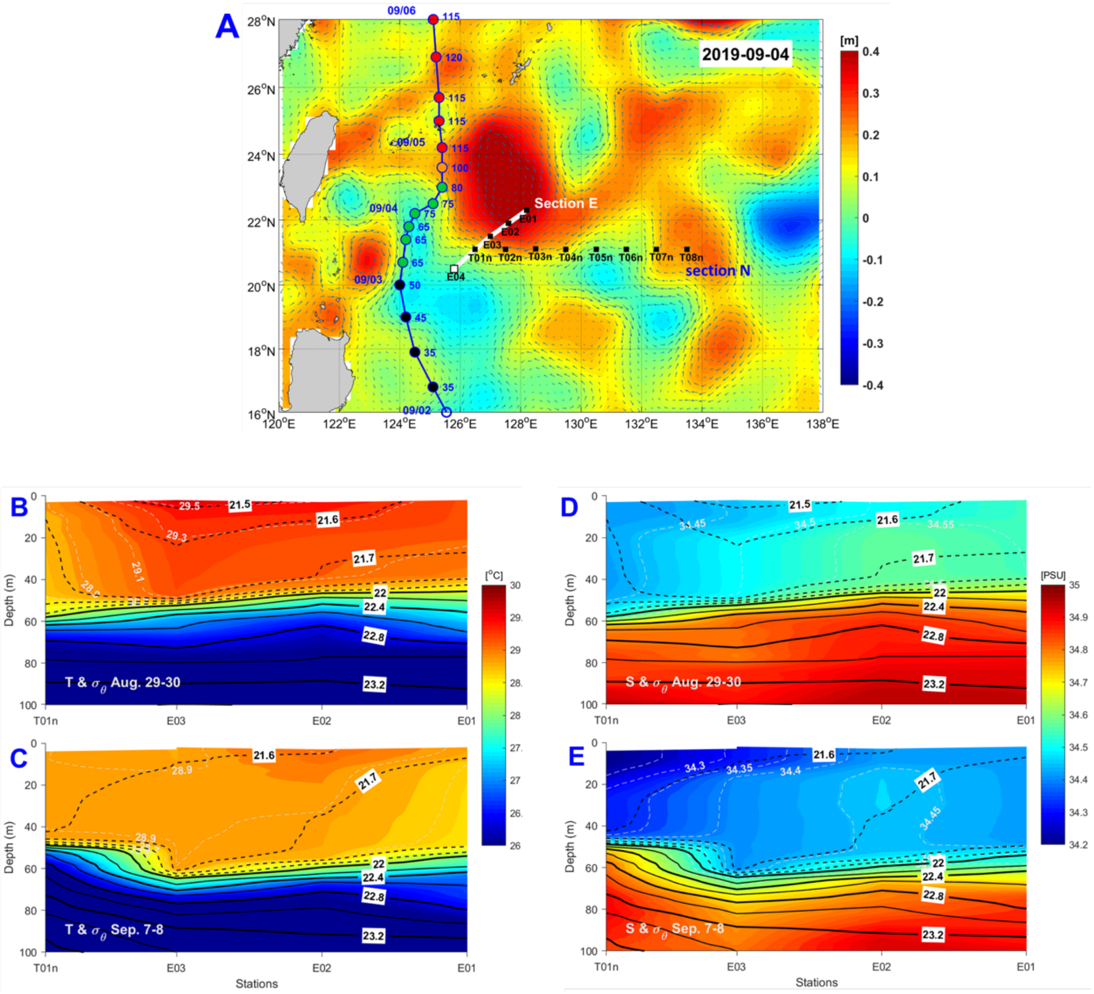

Figure 4.1. (a) Track of TC Lingling with sea surface height anomaly (SSHa) on 4 September 2019, and CTD casting stations (black rectangular). Numbers along track indicate maximum wind speed (knots). Temperature profile of section E (b) before and (c) after Lingling and salinity (d) before and (e) after storm passage. White dotted lines denote isothermal lines, with black solid and dotted lines indicate isopycnal lines at interval of 0.2 and 0.1, respectively.

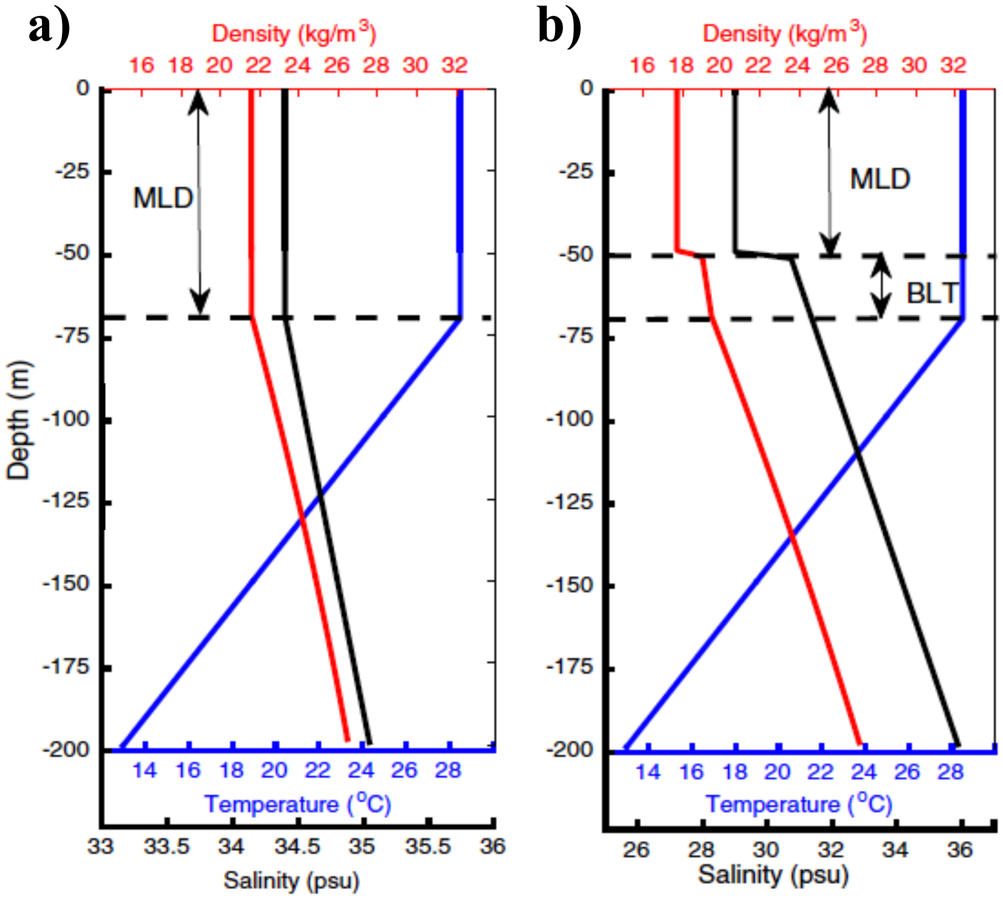

Figure 4.2. Schematic temperature (blue), salinity (black), and density (red) profiles showing the mixed layer depth (MLD) and the barrier layer thickness (BLT). Shown are the cases of (a) no BL and (b) BL (Yan et al., 2017).

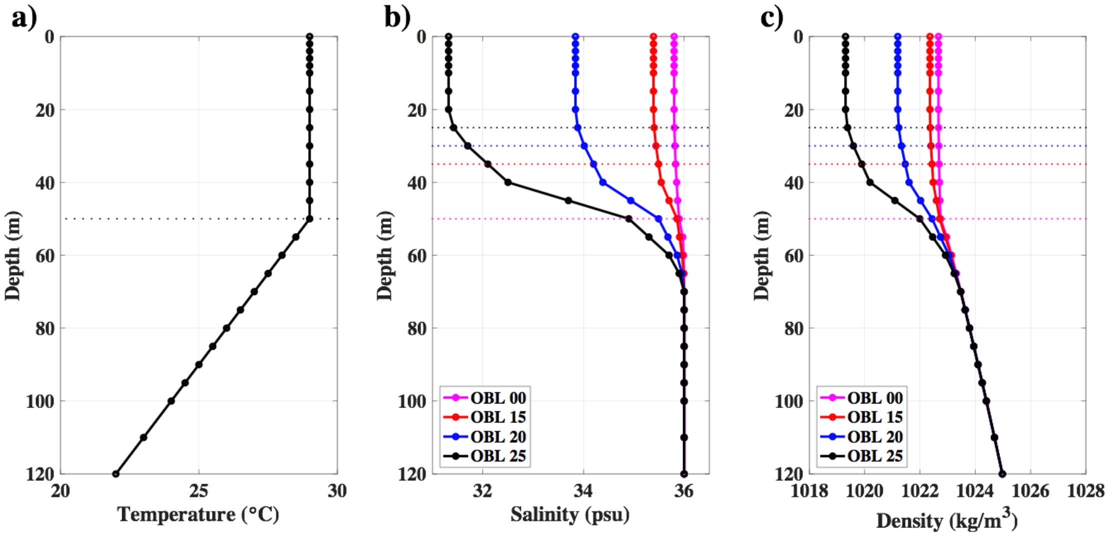

Figure 4.3. Upper 120 m of ocean (a) temperature (°C), (b) salinity (psu), (c) density (kg/m^3) profiles. Dashed lines indicate the ILD in the temperature plot and the different MLDs between each BL case.

Table 5. List of OBL experiments.

	ILD (m)	**MLD (m)**	**OBL (m)**
OBL00	50	50	0
OBL15	50	35	15
OBL20	50	30	20
OBL25	50	25	25

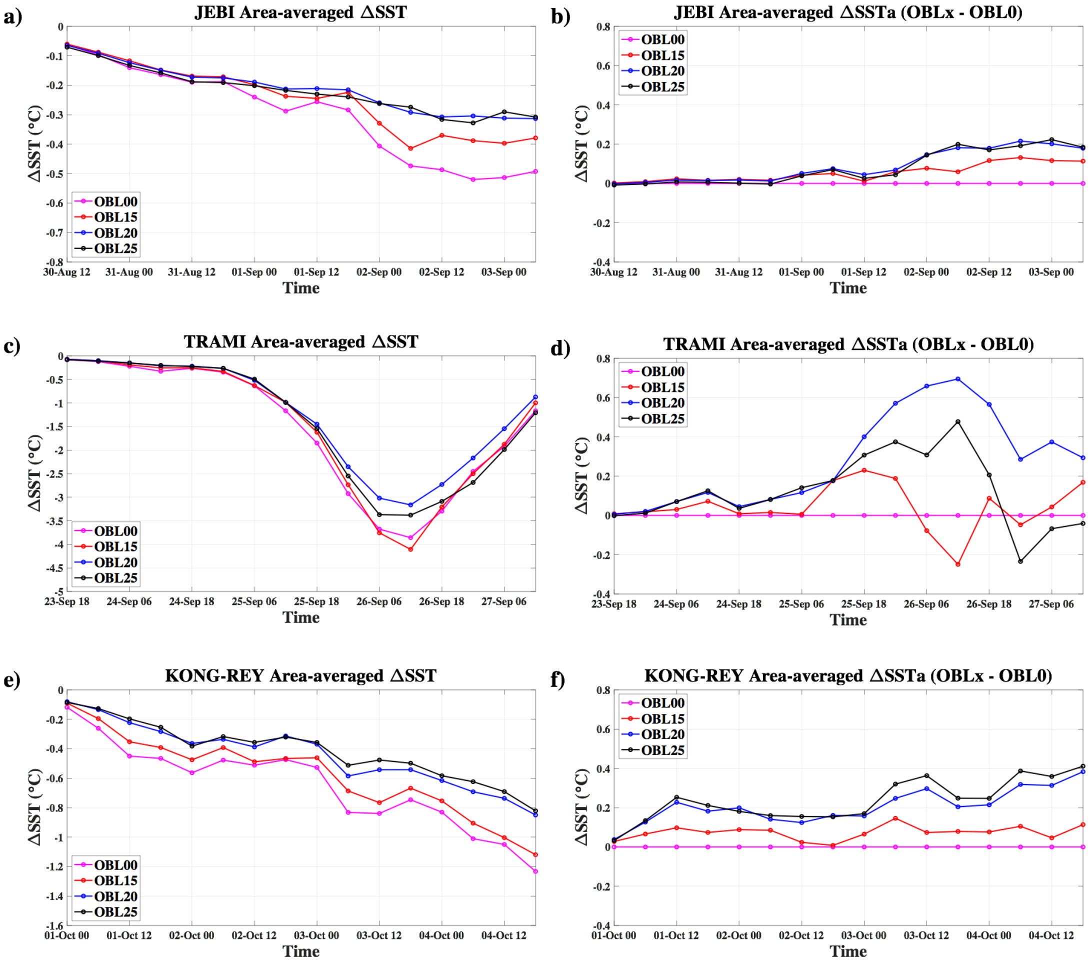

Figure 4.4. Time series of area-averaged ΔSST for each BL case for (a) Jebi, (c) Trami, and (e) Kong-rey, and anomaly between OBLx and OBL00 for (b) Jebi, (d) Trami, and (f) Kong-rey within 100 km of the storm center as a function of time.

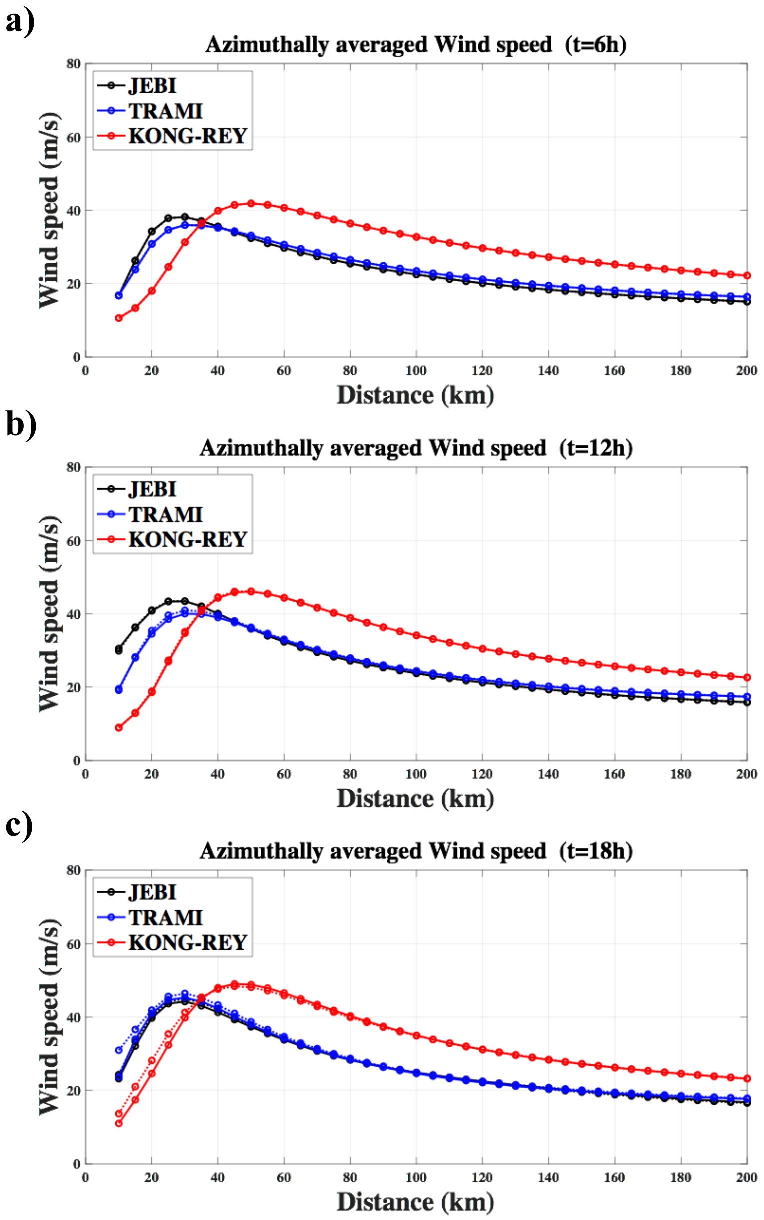

Figure 4.5. Azimuthally averaged wind speed (m/s) every 5 km for Jebi (black), Trami (blue), and Kong-rey (red) at (a) 6 h, (b) 12 h, and 18 h after the simulation begins. Solid lines indicate the OBL00 cases, and dashed lines indicate the OBL25 cases.

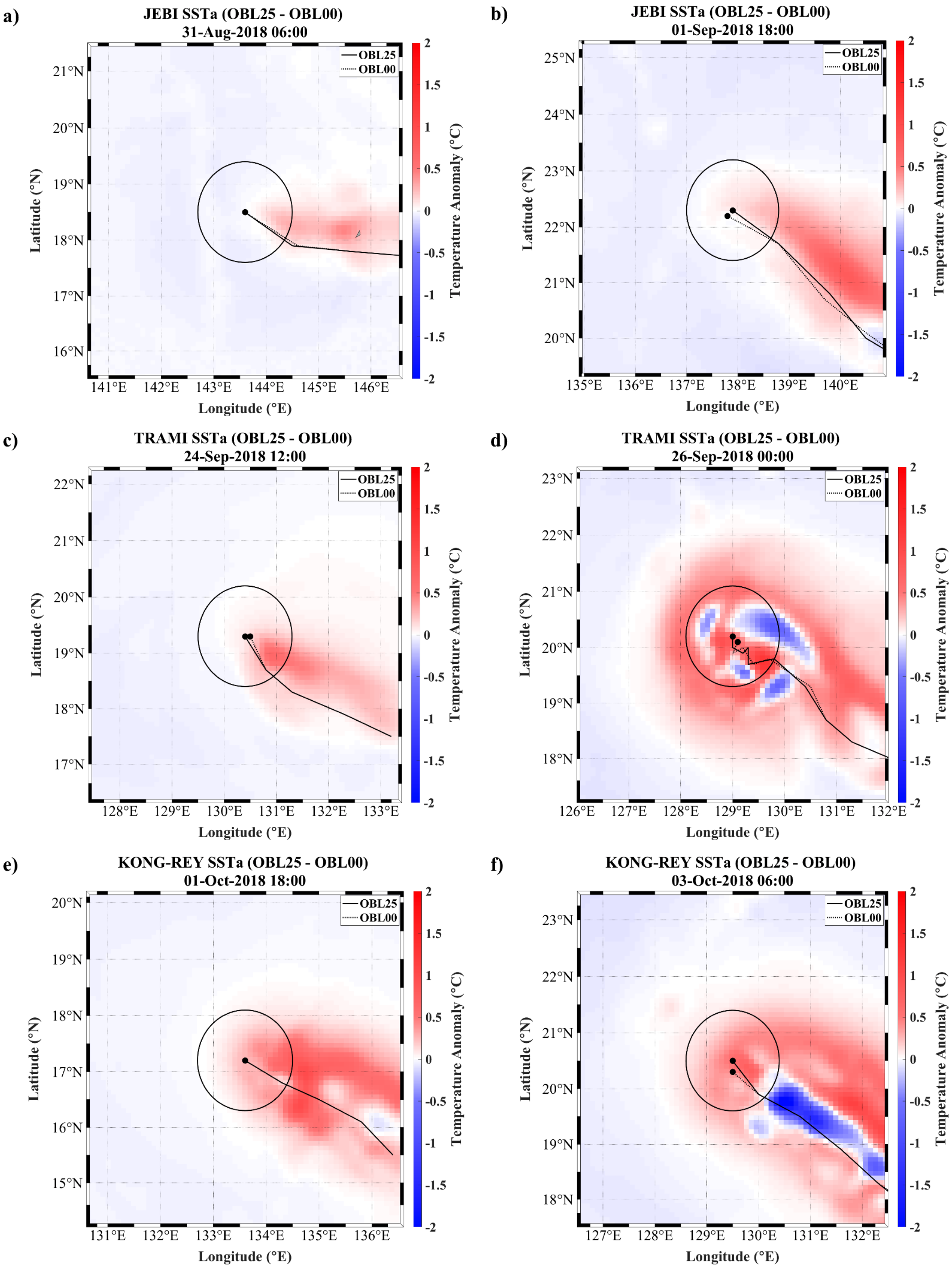

Figure 4.6. Spatial distribution of SST anomaly between OBL25 and OBL00 for (a), (b) Jebi, (c), (d) Trami, and (e), (f) Kong-rey at (left) 24 and (right) 60 h after the simulation begins. Black circle indicates the 100 km radius around the storm center, and black dot indicates the storm center. Solid and dashed lines indicate track of OBL25 and OBL00 experiments, respectively.

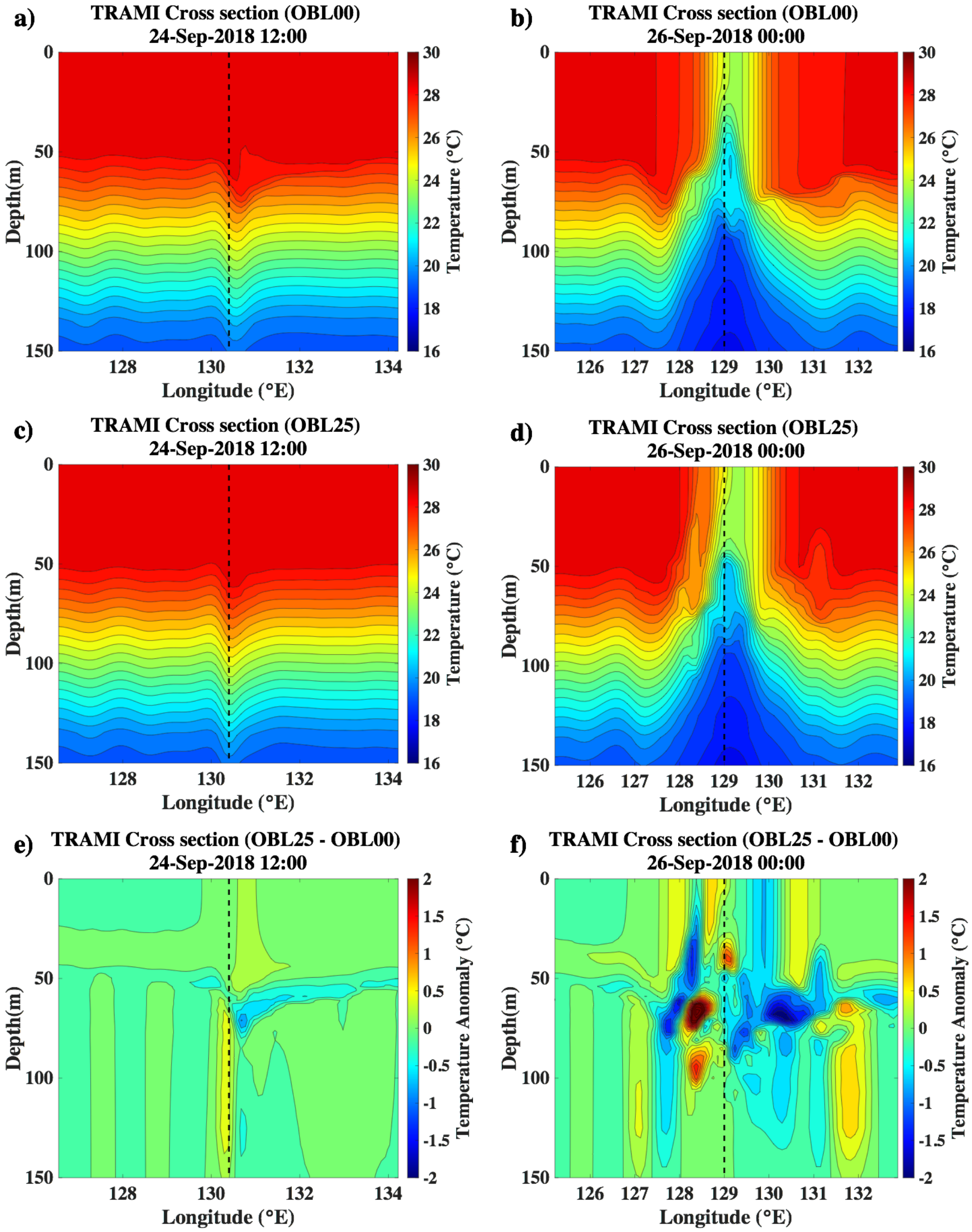

Figure 4.7. Zonal vertical cross section of ocean temperature (a), (b) OBL00 and (c), (d) OBL25 and (e), (f) anomaly (OBL25 - OBL00) at the storm center of OBL25 experiment at (left) 24 and (right) 60 h after the simulation begins.

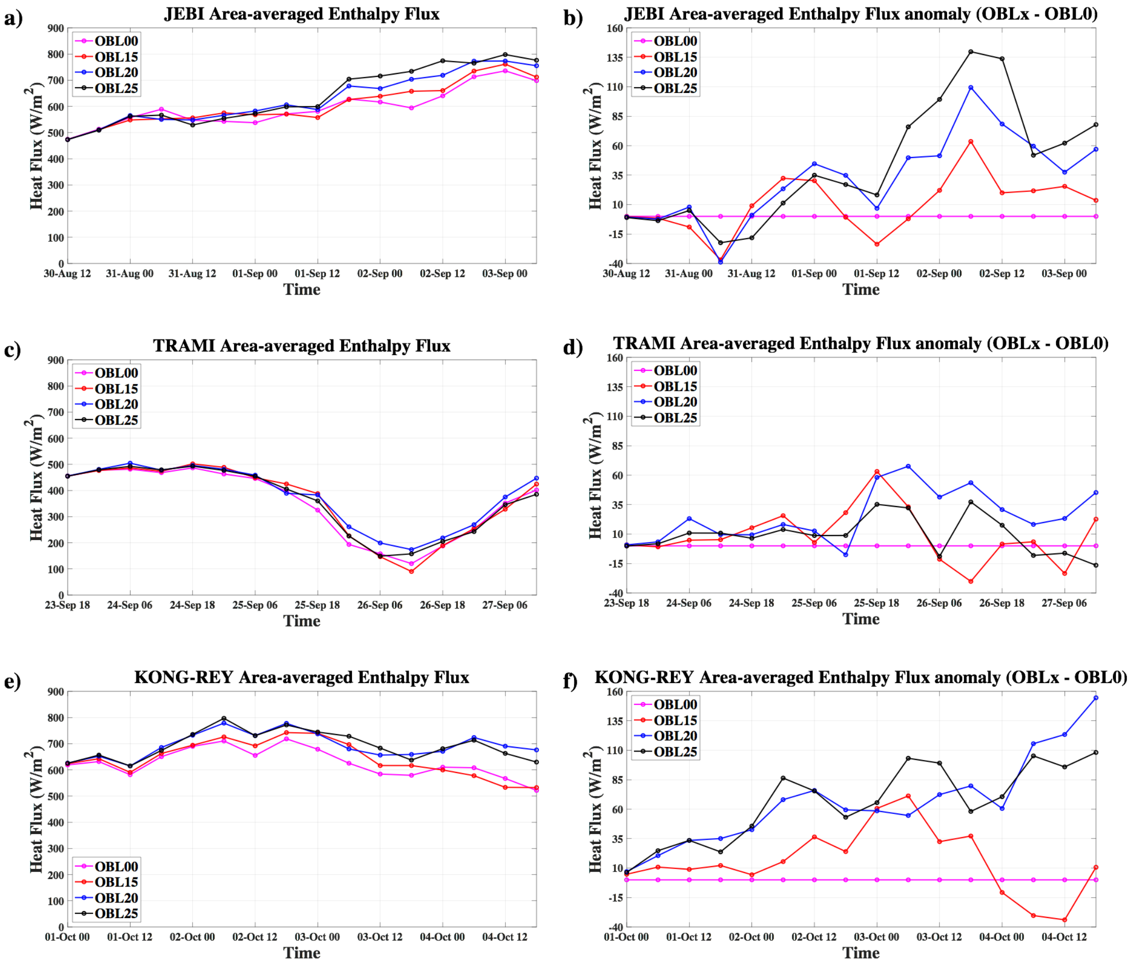

Figure 4.8. Time series of area-averaged enthalpy flux (W/m^2) for each BL case for (a) Jebi, (c) Trami, and (e) Kong-rey, and anomaly between OBLx and OBL00 for (b) Jebi, (d) Trami, and (f) Kong-rey within 100 km of the storm center as a function of time.

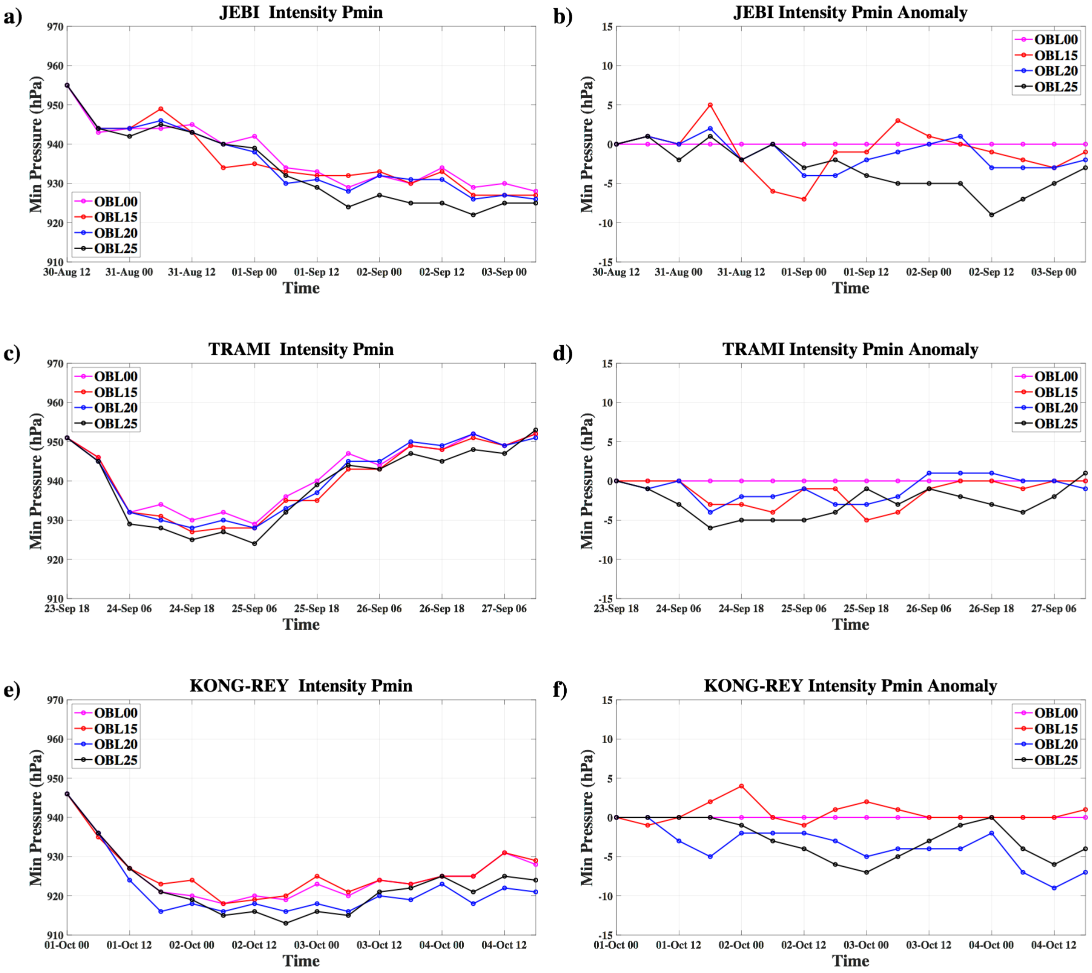

Figure 4.9. Time series of minimum pressure (hPa) for each BL case for (a) Jebi, (c) Trami, and (e) Kong-rey, and anomaly between OBLx and OBL00 for (b) Jebi, (d) Trami, and (f) Kong-rey as a function of time.

Table 6. Maximum different values between
OBLx and OBL00 experiments.

JEBI	OBL15	OBL20	OBL25
ΔSST (°C)	0.13	0.22	0.22
ΔHF (W/m^2)	63.60	109.42	139.78
ΔPmin (hPa)	7	4	9
ΔVmax (m/s)	6.17	6.69	8.75

TRAMI	OBL15	OBL20	OBL25
ΔSST (°C)	0.23	0.70	0.48
ΔHF (W/m^2)	63.15	67.57	37.29
ΔPmin (hPa)	5	4	6
ΔVmax (m/s)	5.67	9.26	5.14

KONG-REY	OBL15	OBL20	OBL25
ΔSST (°C)	0.15	0.38	0.41
ΔHF (W/m^2)	71.24	154.56	108.14
ΔPmin (hPa)	1	9	7
ΔVmax (m/s)	2.57	5.66	6.69

BIBLIOGRAPHY

Anandh, T.S., Das, B.K., Kuttippurath, J. and Chakraborty, A., 2020. A coupled model analyses on the interaction between oceanic eddies and tropical cyclones over the Bay of Bengal. Ocean Dynamics, 70(3), pp.327-337.

Balaguru, K., Chang, P., Saravanan, R., Leung, L.R., Xu, Z., Li, M. and Hsieh, J.S., 2012. Ocean barrier layers' effect on tropical cyclone intensification. *Proceedings of the National Academy of Sciences*, *109*(36), pp.14343-14347.

Bender, M.A. and Ginis, I., 2000. Real-case simulations of hurricane–ocean interaction using a high-resolution coupled model: Effects on hurricane intensity. *Monthly Weather Review*, *128*(4), pp.917-946.

Biswas, M.K., Carson, L., Newman, K., Bernardet, L., Kalina, E., Grell, E. and Frimel, J., 2017. Community HWRF users guide v3. 9a.

Carnes, M.R., 2009. *Description and Evaluation of GDEM-V 3.0* (No. NRL/MR/7330 --09-9165). Naval Research Lab Stennis Space Center Ms Oceanography Div.

Chan, J.C., Duan, Y. and Shay, L.K., 2001. Tropical cyclone intensity change from a simple ocean–atmosphere coupled model. *Journal of the Atmospheric Sciences*, *58*(2), pp.154-172.

Cione, J.J. and Uhlhorn, E.W., 2003. Sea surface temperature variability in hurricanes: Implications with respect to intensity change. *Monthly Weather Review*, *131*(8), pp.1783-1796.

D'Asaro, E.A., Sanford, T.B., Niiler, P.P. and Terrill, E.J., 2007. Cold wake of hurricane Frances. *Geophysical Research Letters*, *34*(15).

de Boyer Montégut, C., Mignot, J., Lazar, A. and Cravatte, S., 2007. Control of salinity on the mixed layer depth in the world ocean: 1. General description. *Journal of Geophysical Research: Oceans*, *112*(C6).

Emanuel, K.A., 1986. An air-sea interaction theory for tropical cyclones. Part I: Steady-state maintenance. *Journal of the Atmospheric Sciences*, *43*(6), pp.585-605.

Emanuel, K., DesAutels, C., Holloway, C. and Korty, R., 2004. Environmental control of tropical cyclone intensity. *Journal of the atmospheric sciences*, *61*(7), pp.843-858.

Emanuel, K., 2005. Increasing destructiveness of tropical cyclones over the past 30 years. *Nature*, *436*(7051), pp.686-688.

Falkovich, A., Ginis, I. and Lord, S., 2005. Ocean data assimilation and initialization procedure for the Coupled GFDL/URI Hurricane Prediction System. *Journal of Atmospheric and Oceanic Technology*, *22*(12), pp.1918-1932.

Ginis, I., 2002. Tropical cyclone-ocean interactions. *Advances in Fluid Mechanics*, *33*, pp.83-114.

Grodsky, S.A., Reul, N., Lagerloef, G., Reverdin, G., Carton, J.A., Chapron, B., Quilfen, Y., Kudryavtsev, V.N. and Kao, H.Y., 2012. Haline hurricane wake in the Amazon/Orinoco plume: AQUARIUS/SACD and SMOS observations. *Geophysical Research Letters*, *39*(20).

Hernandez, O., Jouanno, J. and Durand, F., 2016. Do the Amazon and Orinoco freshwater plumes really matter for hurricane-induced ocean surface cooling?. *Journal of Geophysical Research: Oceans*, *121*(4), pp.2119-2141.

Hlywiak, J. and Nolan, D.S., 2019. The Influence of Oceanic Barrier Layers on Tropical Cyclone Intensity as Determined through Idealized, Coupled Numerical Simulations. *Journal of Physical Oceanography*, *49*(7), pp.1723-1745.

Hong, X., Chang, S.W., Raman, S., Shay, L.K. and Hodur, R., 2000. The interaction between Hurricane Opal (1995) and a warm core ring in the Gulf of Mexico. *Monthly Weather Review*, *128*(5), pp.1347-1365.

Hwang, C., Wu, C.R. and Kao, R., 2004. TOPEX/Poseidon observations of mesoscale eddies over the Subtropical Countercurrent: Kinematic characteristics of an anticyclonic eddy and a cyclonic eddy. *Journal of Geophysical Research: Oceans*, *109*(C8).

Jaimes, B., Shay, L.K. and Uhlhorn, E.W., 2015. Enthalpy and momentum fluxes during Hurricane Earl relative to underlying ocean features. *Monthly Weather Review*, *143*(1), pp.111-131.

Jaimes, B. and Shay, L.K., 2015. Enhanced wind-driven downwelling flow in warm oceanic eddy features during the intensification of Tropical Cyclone Isaac (2012): Observations and theory. *Journal of Physical Oceanography*, *45*(6), pp.1667-1689.

Jaimes, B., Shay, L.K. and Brewster, J.K., 2016. Observed air-sea interactions in tropical cyclone Isaac over Loop Current mesoscale eddy features. *Dynamics of Atmospheres and Oceans*, *76*, pp.306-324.

Kang, S.K., 2021. Trapping of low-salinity tropical water by subtropical warm eddies: a poleward-boosting process of tropical cyclone rapid intensification in the Northwest Pacific (Manuscript submitted for publication).

Leipper, D.F. and Volgenau, D., 1972. Hurricane heat potential of the Gulf of Mexico. *Journal of Physical Oceanography*, *2*(3), pp.218-224.

Lin, I.I., Wu, C.C., Emanuel, K.A., Lee, I.H., Wu, C.R. and Pun, I.F., 2005. The interaction of Supertyphoon Maemi (2003) with a warm ocean eddy. *Monthly Weather Review*, *133*(9), pp.2635-2649.

Lin, I.I., Black, P., Price, J.F., Yang, C.Y., Chen, S.S., Lien, C.C., Harr, P., Chi, N.H., Wu, C.C. and D'Asaro, E.A., 2013. An ocean coupling potential intensity index for tropical cyclones. *Geophysical Research Letters*, *40*(9), pp.1878-1882.

Liu, Y., Dong, C., Guan, Y., Chen, D., McWilliams, J. and Nencioli, F., 2012. Eddy analysis in the subtropical zonal band of the North Pacific Ocean. *Deep Sea Research Part I: Oceanographic Research Papers*, *68*, pp.54-67.

Lukas, R. and Lindstrom, E., 1991. The mixed layer of the western equatorial Pacific Ocean. *Journal of Geophysical Research: Oceans*, *96*(S01), pp.3343-3357.

Ma, Z., Fei, J., Liu, L., Huang, X. and Li, Y., 2017. An investigation of the influences of mesoscale ocean eddies on tropical cyclone intensities. *Monthly Weather Review*, *145*(4), pp.1181-1201.

Mainelli, M., DeMaria, M., Shay, L.K. and Goni, G., 2008. Application of oceanic heat content estimation to operational forecasting of recent Atlantic category 5 hurricanes. *Weather and Forecasting*, *23*(1), pp.3-16.

McTaggart-Cowan, R., Bosart, L.F., Gyakum, J.R. and Atallah, E.H., 2007. Hurricane Katrina (2005). Part I: Complex life cycle of an intense tropical cyclone. *Monthly weather review*, *135*(12), pp.3905-3926.

Mellor, G.L. and Yamada, T., 1982. Development of a turbulence closure model for geophysical fluid problems. *Reviews of Geophysics*, *20*(4), pp.851-875.

Mellor, G.L., 2004. Users guide for a three-dimensional, primitive equation, numerical ocean model (June 2004 version). *Prog. in Atmos. and Ocean. Sci, Princeton University, 56pp.*

Neetu, S., Lengaigne, M., Vincent, E.M., Vialard, J., Madec, G., Samson, G., Ramesh Kumar, M.R. and Durand, F., 2012. Influence of upper-ocean stratification on tropical cyclone-induced surface cooling in the Bay of Bengal. *Journal of Geophysical Research: Oceans*, *117*(C12).

Newinger, C. and Toumi, R., 2015. Potential impact of the colored A mazon and O rinoco plume on tropical cyclone intensity. *Journal of Geophysical Research: Oceans*, *120*(2), pp.1296-1317.

Peduzzi, P., Chatenoux, B., Dao, H., De Bono, A., Herold, C., Kossin, J., Mouton, F. and Nordbeck, O., 2012. Global trends in tropical cyclone risk. *Nature climate change*, *2*(4), pp.289-294.

Price, J.F., 1981. Upper ocean response to a hurricane. *Journal of Physical Oceanography*, *11*(2), pp.153-175.

Price, J.F., 1983. Internal wave wake of a moving storm. Part I. Scales, energy budget and observations. *Journal of Physical Oceanography*, *13*(6), pp.949-965.

Qiu, B., 1999. Seasonal eddy field modulation of the North Pacific Subtropical Countercurrent: TOPEX/Poseidon observations and theory. *Journal of Physical Oceanography*, *29*(10), pp.2471-2486.

Reul, N., Chapron, B., Lee, T., Donlon, C., Boutin, J. and Alory, G., 2014. Sea surface salinity structure of the meandering Gulf Stream revealed by SMOS sensor. *Geophysical Research Letters*, *41*(9), pp.3141-3148.

Reynolds, R.W. and Smith, T.M., 1994. Improved global sea surface temperature analyses using optimum interpolation. *Journal of climate*, *7*(6), pp.929-948.

Roemmich, D. and Gilson, J., 2001. Eddy transport of heat and thermocline waters in the North Pacific: A key to interannual/decadal climate variability?. *Journal of Physical Oceanography*, *31*(3), pp.675-687.

Rudzin, J.E., Shay, L.K. and Johns, W.E., 2018. The influence of the barrier layer on SST response during tropical cyclone wind forcing using idealized experiments. *Journal of Physical Oceanography*, *48*(7), pp.1471-1478.

Schade, L.R. and Emanuel, K.A., 1999. The ocean’s effect on the intensity of tropical cyclones: Results from a simple coupled atmosphere–ocean model. *Journal of the Atmospheric Sciences*, *56*(4), pp.642-651.

Shay, L.K., Elsberry, R.L. and Black, P.G., 1989. Vertical structure of the ocean current response to a hurricane. *Journal of physical oceanography*, *19*(5), pp.649-669.

Shay, L.K., Goni, G.J. and Black, P.G., 2000. Effects of a warm oceanic feature on Hurricane Opal. *Monthly Weather Review*, *128*(5), pp.1366-1383.

Shen, W. and Ginis, I., 2003. Effects of surface heat flux-induced sea surface temperature changes on tropical cyclone intensity. *Geophysical research letters*, *30*(18).

Sprintall, J. and Tomczak, M., 1992. Evidence of the barrier layer in the surface layer of the tropics. *Journal of Geophysical Research: Oceans*, *97*(C5), pp.7305-7316.

Sun, J., Wang, G., Xiong, X., Hui, Z., Hu, X., Ling, Z., Yu, L., Yang, G., Guo, Y., Ju, X. and Chen, L., 2020. Impact of warm mesoscale eddy on tropical cyclone intensity. *Acta Oceanologica Sinica*, *39*(8), pp.1-13.

Tallapragada, V., Bernardet, L., Biswas, M.K., Gopalakrishnan, S., Kwon, Y., Liu, Q., Marchok, T., Sheinin, D., Tong, M., Trahan, S. and Tuleya, R., 2014. Hurricane Weather Research and Forecasting (HWRF) model: 2013 scientific documentation. *NCAR HWRF Development Testbed Center Tech. Rep*.

Teague, W.J., Carron, M.J. and Hogan, P.J., 1990. A comparison between the Generalized Digital Environmental Model and Levitus climatologies. *Journal of Geophysical Research: Oceans*, *95*(C5), pp.7167-7183.

Trahan, S. and Sparling, L., 2012. An analysis of NCEP tropical cyclone vitals and potential effects on forecasting models. Weather and forecasting, 27(3), pp.744-756.

Vianna, M.L., Menezes, V.V., Pezza, A.B. and Simmonds, I., 2010. Interactions between Hurricane Catarina (2004) and warm core rings in the South Atlantic Ocean. *Journal of Geophysical Research: Oceans*, *115*(C7).

Vissa, N.K., Satyanarayana, A.N.V. and Kumar, B.P., 2013. Response of upper ocean and impact of barrier layer on Sidr cyclone induced sea surface cooling. *Ocean Science Journal*, *48*(3), pp.279-288.

Wang, X., Han, G., Qi, Y. and Li, W., 2011. Impact of barrier layer on typhoon-induced sea surface cooling. *Dynamics of Atmospheres and Oceans*, *52*(3), pp.367-385.

Wang, G., Zhao, B., Qiao, F. and Zhao, C., 2018. Rapid intensification of Super Typhoon Haiyan: the important role of a warm-core ocean eddy. *Ocean Dynamics*, *68*(12), pp.1649-1661.

Wu, C.C., Lee, C.Y. and Lin, I.I., 2007. The effect of the ocean eddy on tropical cyclone intensity. *Journal of the Atmospheric Sciences*, *64*(10), pp.3562-3578.

Yablonsky, R.M. and Ginis, I., 2008. Improving the ocean initialization of coupled hurricane–ocean models using feature-based data assimilation. *Monthly Weather Review*, *136*(7), pp.2592-2607.

Yablonsky, R.M. and Ginis, I., 2009. Limitation of one-dimensional ocean models for coupled hurricane–ocean model forecasts. *Monthly Weather Review*, *137*(12), pp.4410-4419.

Yablonsky, R.M. and Ginis, I., 2013. Impact of a warm ocean eddy's circulation on hurricane-induced sea surface cooling with implications for hurricane intensity. *Monthly weather review*, *141*(3), pp.997-1021.

Yablonsky, R.M., Ginis, I., Thomas, B., Tallapragada, V., Sheinin, D. and Bernardet, L., 2015. Description and analysis of the ocean component of NOAA's

Operational Hurricane Weather Research and Forecasting Model (HWRF). *Journal of Atmospheric and Oceanic Technology*, *32*(1), pp.144-163.

Yan, Y., Li, L. and Wang, C., 2017. The effects of oceanic barrier layer on the upper ocean response to tropical cyclones. *Journal of Geophysical Research: Oceans*, *122*(6), pp.4829-4844.

Yang, G., Wang, F., Li, Y. and Lin, P., 2013. Mesoscale eddies in the northwestern subtropical Pacific Ocean: Statistical characteristics and three-dimensional structures. *Journal of Geophysical Research: Oceans*, *118*(4), pp.1906-1925.